IS-T--1410

DE91 000662

High-resolution Angle-resolved Photoemission Studies of High T*c* Superconductor Bi*2*Sr*2*CaCu*2*O*8*

by

Liu, Rong

PHD Thesis submitted to Iowa State University

Ames Laboratory, U.S. DOE

Iowa State University

Ames, Iowa 50011

Date Transmitted: September 21, 1990

PREPARED FOR THE U.S. DEPARTMENT OF ENERGY

UNDER CONTRACT NO. W-7405-Eng-82.

MASTER

DISCLAIMER

High-resolution angle-resolved photoemission studies of high T_c superconductor $Bi_2Sr_2CaCu_2O_8$

Rong Liu

Under the supervision of David W. Lynch
From the Department of Physics
Iowa State University

An angle-resolved photoemission study of the normal and super-conducting states in $Bi_2Sr_2CaCu_2O_8$ was performed. Measurements in the normal state show bands dispersing through the Fermi level from at least 350 meV below E_F. The Fermi level crossings are consistant with local-density band calculation, including a point calculated to be of Bi-O character. Additional measurements were made where bands crossed the Fermi level between 100 and 250K, along with measurements on an adjacent Pt foil. The Fermi edges of both materials agree to within the noise. Below the Fermi level, the spectra show correlation effects in the form of an increased effective mass. The shape of the spectra can be explained by a lifetime-broadened photohole and secondary electrons. The effective inverse photohole lifetime is linear in energy. A superconducting gap has been measured at a number of points where there is density at the Fermi level in the normal state. By proper modeling, a gap of 24 meV was obtained for all these points, including points of Cu-O and Bi-O character respectively, according to band calculation. The lack of gap anisotropy in the basal plane suggests that pairing in this material is not d-wave pairing.

High-resolution angle-resolved photoemission studies of

high T_c superconductor $Bi_2Sr_2CaCu_2O_8$

by

Rong Liu

A Dissertation Submitted to the

Graduate Faculty in Partial Fulfillment of the

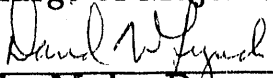Requirements for the Degree of

DOCTOR OF PHILOSOPHY

Department: Physics

Major: Solid State Physics

Approved:

In Charge of Major Work

For the Major Department

For the Graduate College

Iowa State University

Ames, Iowa

1990

TABLE OF CONTENTS

I. INTRODUCTION

A. Brief History and Some Common Properties

Superconductivity is a phenomenon in which the DC resistivity of certain materials drops to zero below a critical temperature. At the same time, these materials display perfect diamagnetism in a weak magnetic field. This phenomenon was first discovered by Kammerlingh Onnes in 1911 in Hg at 4.2K. In order to make superconductivity of practical use, materials with high enough transition temperatures (T_c) are desired. However, in more than seven decades, the progress of the search for high T_c superconductors was very slow. The highest T_c ever achieved before 1986 is 23K in Nb_3Ge. And this was widely believed to be near the limit in a classical BCS coupling scheme.

The first breakthrough came in 1986 when Bednorz and Müller found T_c of 30K in the La-Ba-Cu-O system [1]. This result was soon confirmed by many other groups in the world. In the following year or two, many other related superconductors with much higher values of T_c were found. At present, there are four major groups of high T_c superconductors: (1) The original La-Cu-O system with various doping, with T_c in the $30-40K$ range; (2) $RBa_2Cu_3O_{7-\delta}$ (123) [2] with $T_c \sim 90K$, where R = rare earth; (3) the Bi-Sr-Ca-Cu-O [3] and Tl-Sr-Ca-Cu-O [4] systems with T_c up to 125K; (4) the Nd-Ce-Cu-O system [5], the so-called n-type superconductor with $T_c \sim 30-40K$.

These various high T_c superconductors have many properties in common. First, they all have a perovskite-like crystal structure, which

consists of Cu-O sheets separated by more or less ionic layers. Secondly, all these compounds have copper and oxygen as common constituents It is widely believed that the superconducting charge carriers are from the Cu-O sheets. Thirdly, all these compounds are quasi two-dimensional, in other words, the interplane coupling is very small. As a result, there is strong anisotropy in many of their properties. For example, resistivity measurements [6] showed metallic behavior along the a- and b-axes, and insulating behavior along the c-axis. Tunneling [7] and infrared [8] measurements found a larger superconducting gap in the plane than perpendicular to the plane. It is very likely that the two-dimensionality is a key factor in understanding many of the anomalous behaviors these materials exhibit in their normal and superconducting states [9].

B. The BCS Theory

Conventional superconductors are successfully explained by the BCS (Bardeen-Cooper-Schrieffer) theory [10]. The basic ingredients of this theory are the following: (1) a net attractive interaction between electrons in the neighborhood of the Fermi surface, which occurs via an exchange of virtual phonons; (2) in the presence of such a net attractive interaction, two electrons at the Fermi surface (while the other $N - 2$ electrons fill the Fermi sea) form a bound pair (so-called Cooper pair) [11]; (3) the normal metallic state is unstable with respect to formation of a macroscopic condensed state of all pairs with opposite momentum $(\mathbf{k}, -\mathbf{k})$.

The main quantitative predictions of the BCS theory are:

In the weak coupling limit ($\rho V \ll 1$), the zero-temperature energy gap is given by

$$\Delta_0 = 2\hbar\omega_D \cdot exp(-1/\rho V), \qquad (1.1)$$

where ρ is the density of states at the Fermi level, V is the phonon mediated electron-electron coupling.

The superconducting transition temperature T_c is given by

$$T_c = 1.14\Theta_D \cdot exp(-1/\rho V). \qquad (1.2)$$

Because of the the presence of the exponential factor in equation (1.2), the critical temperature T_c is much smaller than the Debye temperature. In fact, for $\rho V \ll 1$, T_c up to 25K should be very exceptional. This led many people to believe that T_c=23K in Nb_3Ge is the maximum one could hope for in a weak-coupling BCS theory.

The ratio of Eqns. (1.1) and (1.2) gives a fundamental formula independent of the phenomenological parameters:

$$2\Delta_0/kT_c = 3.53. \qquad (1.3)$$

This result holds for a large number of conventional superconductors to within about ten percent. Deviations from this can usually be explained by strong-coupling effects [12].

Although the BCS theory is succesful in conventional superconductors, it met several apparent difficulties in the new high T_c superconductors. First of all, the high value of T_c cannot be explained by equation (1.2). Second, the ratio Δ_0/kT_c is usually found to be in the range between 6 and 8, substantially greater than 3.53. This

has encouraged many people to look for other mechanisms of super-conductivity. However, whether BCS theory is relevant or not is not clear. In a review paper [9], Friedel showed that a large value of T_c can be explained in a standard BCS weak-coupling scheme for delocalized electrons, if one takes into account the presence of large van Hove anomalies in the density of states near the Fermi level, due to the quasi two-dimensional structure of the oxides.

C. The Electronic Structure of High T_c Superconductors

The normal states of conventional superconductors are well described by band theory. By contrast, the high T_c oxides are much more complicated. The main issue is whether a localized picture or a delocalized picture is more suitable for these oxides, and whether a Fermi liquid description is valid. A localized picture was preferred by many people shortly after the discovery of high T_c superconductors for several reasons. First, band calculations fail to predict that La_2CuO_4 and $YBa_2Cu_3O_6$ are insulators [13]. This is very similar to the situation in transition metal oxides, which was a long standing and interesting problem before the high T_c materials were found [14]. Secondly, a Cu valence band satellite was observed in photoemission experiments, a feature usually associated with many-body effects. Furthermore, early photoemission experiments on 123 samples usually observed a very low density of states at the Fermi level and a 2 eV rigid shift of the valence band toward higher binding energy compared to band calculations [15]. These results encouraged many people to think that Fermi liquid theory is not valid in these systems and a strongly

correlated theory is needed [16, 17].

Later it was shown that the low density of states at the Fermi level and the rigid shift of the valence band observed in photoemission are artifacts of degraded sample surfaces, rather than the intrinsic properties of the material. By cleaving single crystals at 20K, Arko et al. [18] observed distinct Fermi edges. The valence band is also in much closer agreement with band calculations. Besides photoemission experiments, positron annihilation has detected a Fermi surface [19], and NMR experiments also provided evidence for a Fermi liquid behavior [20]. However, the Cu satellite has proved to be intrinsic rather than an artifact. Therefore, correlation effects do exist. Now the question is how important are the correlation effects? Do they dominate the picture, or only alter the Fermi liquid picture slightly?

In order to answer these questions, more experimental data about the electronic structures of these materials are needed. Among many experimental techniques that can be used to probe electronic structures, photoemission with synchrotron radiation is unique in its directness and versatility. In particular, angle-resolved photoemission is especially powerful in revealing detailed information on the electronic structures of solids.

D. Purpose of This Study

The purpose of this study is to use angle-resolved photoemission to investigate the nature of the states near the Fermi level in high T_c superconductors in both normal and superconducting states. For the normal state, the question we try to address is whether Fermi liquid

theory is valid or not, and what are the deviations from the Fermi
liquid theory. For the superconducting state, we measure the super-
conducting gap as the sample is cooled below T_c, and study whether
there is gap anisotropy in the basal plane. For these studies, the rele-
vant energy range is few hundred milivolts below the Fermi level. The
experiments are performed with high energy and angular resolution,
which is essential for studying the details in this small region of in-
terest. Most of the measurements are made on $Bi_2Sr_2CaCu_2O_8$ single
crystals because of sample availability, and also because they are quite
stable at elevated temperatures.

In the following chapters, a brief background of photoemission
will be given first. The phenomena relevant to our experiments will
be discussed in more detail. The experimental details will be given in
Chapter Three. The results and discussion are divided into two ma-
jor parts, the normal state and superconducting state studies. In the
end, I will give an overall summary and discuss some possible future
directions.

II. PHOTOEMISSION

A. Basic Phenomenon and the Three-step Model

Figure 1 illustrates the photoemission process in a solid, in which a photon of energy $h\nu$ is absorbed by an electron in an initial state with eigenenergy E_i, and the electron is excited into an unoccupied state with energy E_f. If the photon energy $h\nu$ is high enough, this energy gain will allow the electron to escape from the solid with a kinetic energy $E_K = E_f - E_v$, according to the well-known Einstein relation [21].

The importance of this phenomenon is that the emitted electron carries information about its initial state before it is ejected. By analyzing the emitted electron as a function of energy, momentum, or spin, information about the electronic structure of the system can be obtained.

Photoemission data are often interpreted by a semi-classical model, the so-called three-step model [22]. In this model, the one-step photoemission process is decomposed as three separate steps: (1) the excitation of the electron with the absorption of the photon, (2) the transport of the excited electron through the solid to the surface, and (3) the escape of the electron from the solids.

Most of the information we are interested in is contained in the first step, the photoexcitation process. Photoexcitation results from the coupling between electrons and the photon field. We shall assume that the photon field in the solid is known, and the perturbing term in
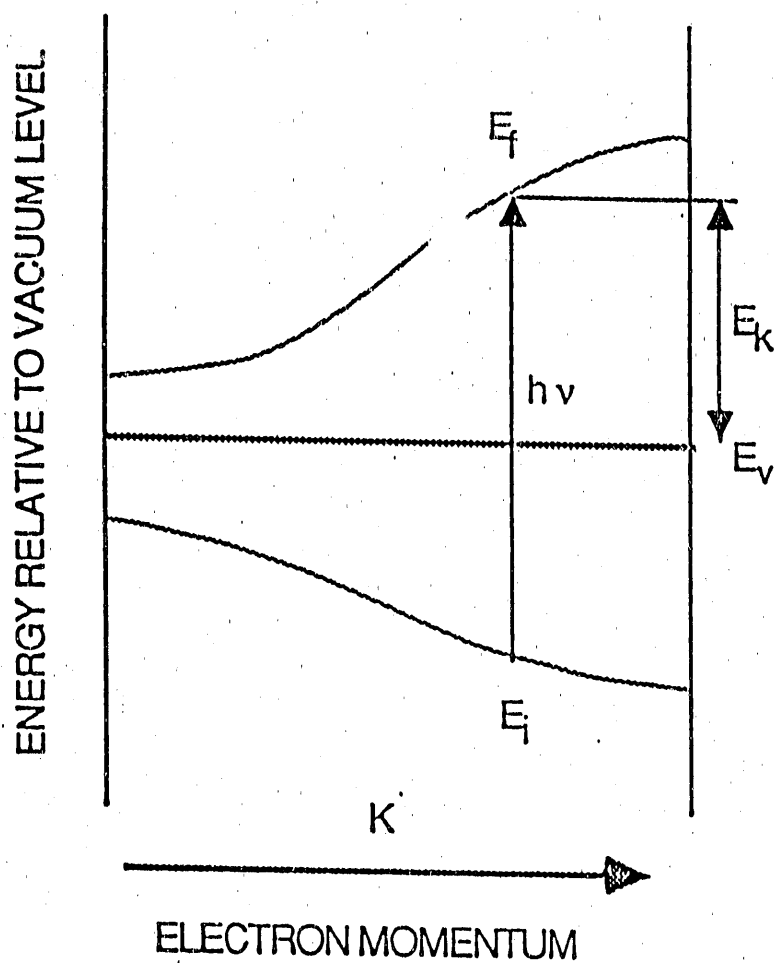
Fig. 1. A direct transition in k-space between an initial band i and final band f giving rise to the emission of a photoelectron of kinetic energy $E_f - E_v$, where E_v is the vacuum level

the Hamiltonian to first order is

$$\Delta = \frac{1}{2c}(\mathbf{p} \cdot \mathbf{A} + \mathbf{A} \cdot \mathbf{p}), \qquad (2.1)$$

where $\mathbf{p}$ is the momentum operator and $\mathbf{A}$ is the field vector. If we neglect the local field and surface effects, we can choose the Coulomb gauge

$$\nabla \cdot \mathbf{A} = 0, \qquad (2.2)$$

so that $\mathbf{p}$ commutes with $\mathbf{A}$. Suppose that the initial and final states are known. Using time-dependent perturbation theory, the excitation probability is given by the Fermi golden-rule

$$W_{if} \sim | < f|\mathbf{A} \cdot \mathbf{p}|i > |^2 \delta(E_f(\mathbf{k}) - E_i(\mathbf{k}) - h\nu), \qquad (2.3)$$

where $|i >$ and $|f >$ are the initial and final state wavefunctions, respectively. It is assumed that the initial state is occupied and the final state is unoccupied. The factor

$$< f|\mathbf{A} \cdot \mathbf{p}|i > \equiv M_{if} \qquad (2.4)$$

is often called the matrix element, and the δ-function ensures conservation of energy. Equation (2.3) also implies conservation of momentum, that is, $\mathbf{k}_f = \mathbf{k}_i$. Therefore, only vertical transitions are considered, such as the one illustrated in Fig. 1.

In the experiment, if the photon energy is fixed and the kinetic energy of the photoelectrons is scanned, the measured spectrum is the energy distribution curve (EDC), which is related to the quantity

$$I(E, \mathbf{k}) \sim |M_{if}|^2 \delta(E_f(\mathbf{k}) - E_i(\mathbf{k}) - h\nu)\delta(E - E_f(\mathbf{k})). \qquad (2.5)$$

In an angle-integrated photoemission experiment, the measured spectrum is the energy distribution of the joint density of states modulated by the matrix element

$$I(E) \sim \int_{BZ} d^3k |M_{if}|^2 \delta(E_f(\mathbf{k}) - E_i(\mathbf{k}) - h\nu)\delta(E - E_f(\mathbf{k})), \quad (2.6)$$

where the integral is over the whole Brillouin zone.

Matrix elements have important effects on photoemission spectra of solids. This is manifested through the spectral dependence on photon energy, due to the details of the initial and final state wavefunctions. In extreme cases, certain transitions can be forbidden because of symmetry if polarized light is used. These effects can be easily observed by using a synchrotron radiation light source.

Now, let us discuss briefly the transport (step 2 in the three-step model) and the escape (step 3 in the three-step model) processes. Both of these processes contribute a smooth function of E to the spectrum and do not introduce structure to the spectrum. The transport process, however, plays an important role in photoelectron spectroscopy, as will be described in the following. In the process of migrating to the surface, the electron is subject to inelastic scattering with other electrons, phonons and plasmons. Such scattering introduces a finite mean free path for the electron. It was found that the mean free paths do not vary much from material to material, and their kinetic energy dependence approximately follows a 'universal' curve as shown in Fig. 2 [23-26]. We see from Fig. 2 that, in the energy range of interest, the electron mean free path is about 5-20 Å. This makes photoemission a very surface-sensitive probe. The high degree of surface sensitivity is both an advantage and a disadvantage.
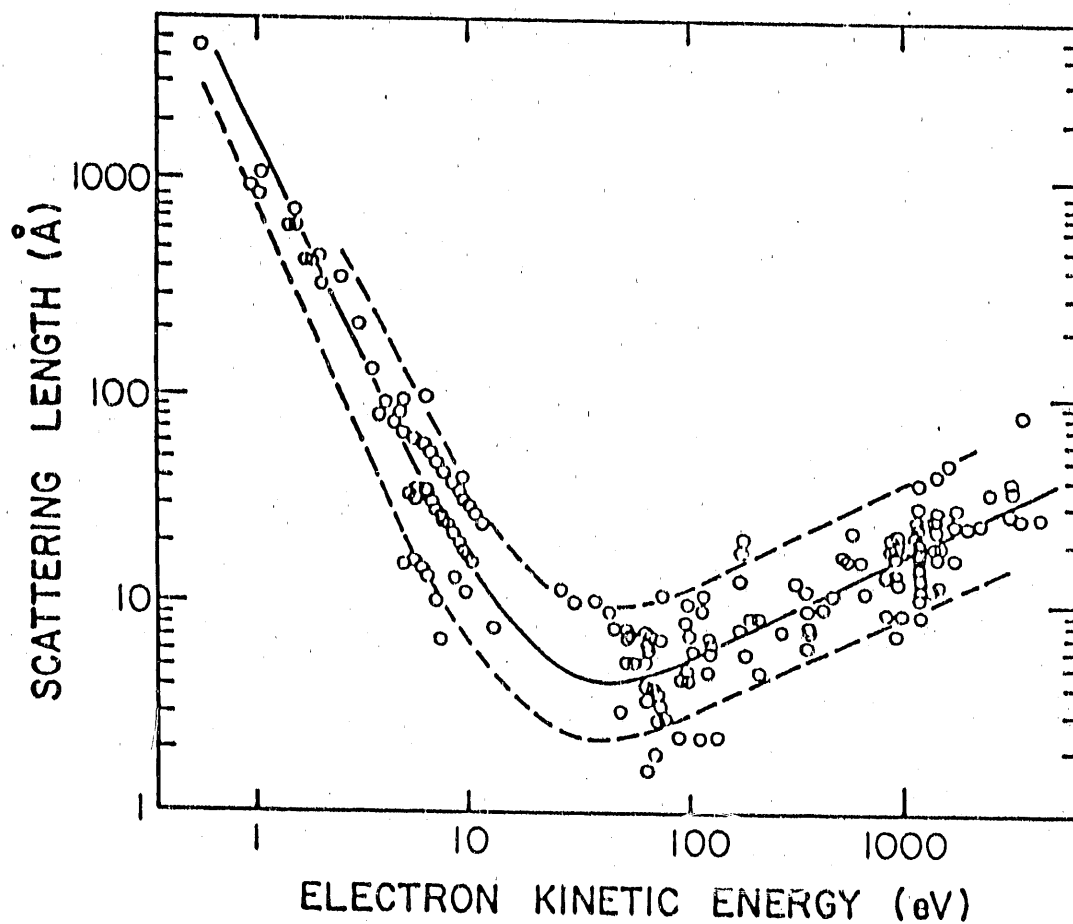
Fig. 2. The "universal curve" showing the photoelectron scattering length or mean free path as a function of its kinetic energy. The circles correspond to results for the scattering lengths for different materials and show the spread in scattering length (Ref. 25)

On the one hand, we can study the surface and near-surface effects. On the other, surface contamination or degradation can distort the photoelectron spectra or contribute non-intrinsic, contamination-derived features. The inelastic scattering also generates secondary electrons which produce a smooth background to the primary electrons of interest.

Although the three-step model is conceptually simple and straightforward, a formal treatment is the so-called one-step model [27-33]. In this model, the photoemission process is considered as a single quantum mechanical event. A particularly elegant formalism is provided by Pendry [31], in which surface effects, matrix element effects and scattering are all naturally included.

B. Angle-resolved Photoemission

In angle-resolved photoemission studies, one analyzes only photoelectrons emitted in a relatively small solid angle (Fig. 3). By knowing the direction of propagation as well as the kinetic energy of the photoelectron, one automatically knows the momentum or wave vector **k**. This follows from the simple relation $E = \hbar^2 k^2 / 2m$ for electrons in vacuo. Therefore, one can isolate one point in k-space rather than sampling the whole Brillouin zone.

Let us suppose that the electron propagates towards the surface and arrives without scattering. Upon escaping across the surface, the parallel component of the wave vector is conserved. The normal component of the wave vector will be reduced due to the potential barrier
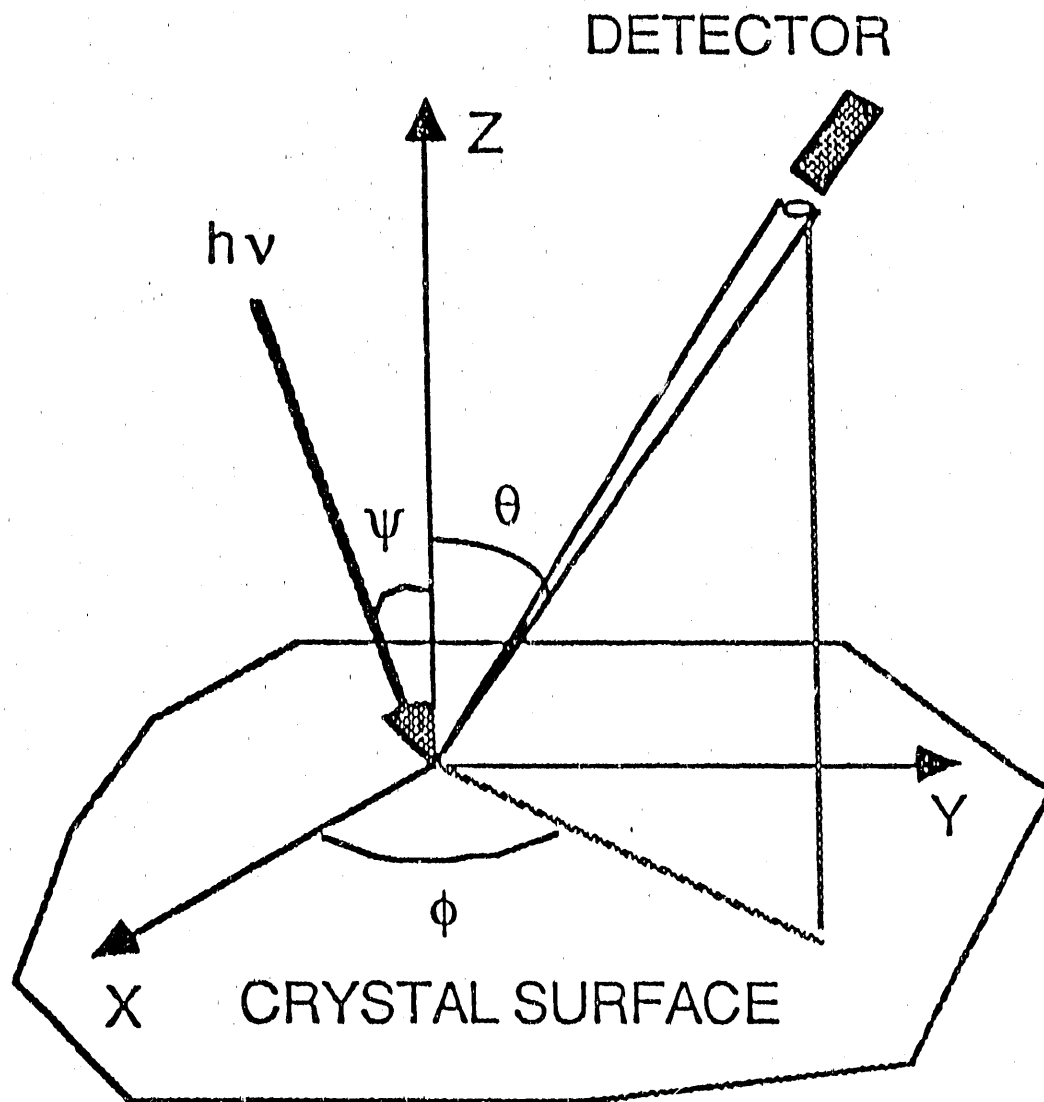
Fig. 3. Illustration of an angle-resolved photoemission experimental configuration

at the surface. Thus, we have

$$\mathbf{k}'_\parallel = \mathbf{k}_\parallel \qquad (2.7)$$

and

$$\hbar^2(\mathbf{k}'^2_\parallel + \mathbf{k}'^2_\perp)/2m = \hbar^2(\mathbf{k}^2_\parallel + \mathbf{k}^2_\perp)/2m - eW, \qquad (2.8)$$

where $\mathbf{k}'_\parallel$, $\mathbf{k}'_\perp$, $\mathbf{k}_\parallel$ and $\mathbf{k}_\perp$ are the parallel and normal components of the external and internal photoelectron wave vector, respectively, and W is the depth of the surface potential barrier.

From a first look, it appears that Eqs. (2.7) and (2.8) relate the $\mathbf{k}$ vectors inside and outside the solid, and one can thus determine the band dispersion $E(\mathbf{k})$ experimentally. Unfortunately, however, we have no detailed knowledge of the surface barrier which in general is energy dependent. That means $\mathbf{k}_\perp$ can not be determined from these two equations. This causes fundamental difficulties in the desire to determine the full three-dimensional band dispersion experimentally. However, there are a number of special situations in which these difficulties are removed. Layered compounds are one of the simple cases. In layered compounds, the dispersion of the energy bands as a function of $\mathbf{k}_\perp$ should be rather small. The energy dispersion then depends almost exclusively on $\mathbf{k}_\parallel$, and the indeterminacy of $\mathbf{k}_\perp$ is no longer a problem. This property is especially advantageous for the study of high T_c superconductors since almost all of them have layered structures. The other simple situation is normal emission. In that case, one can do band mapping in the direction normal to the surface by changing the photon energy.

C. Other Effects in Photoemission

1. Lifetime broadening

In the photoemission process a photoelectron is created, leaving behind a photohole below the Fermi level. The electrons and holes are subject to scattering and have finite lifetimes. In the absence of lifetime effects, and for perfect angle and energy resolution in the analyzer, interband transitions would appear as infinitely sharp peaks in the spectra. With a finite lifetime, the infinitely sharp peak becomes a Lorentzian function

$$I(E) = \alpha \frac{\Gamma}{(E - E_0)^2 + \Gamma^2} \tag{2.9}$$

where Γ is the effective inverse lifetime. The width of the peak is given by

$$\Delta E = 2\Gamma \tag{2.10}$$

Generally, both photoelectron lifetimes and photohole lifetimes contribute to the peak broadening. The effective peak width is [34]

$$\Gamma = \left| \frac{\Gamma_h + R_\perp \Gamma_e}{1 - R_\perp} \right| \tag{2.11}$$

where $R_\perp = |v_{h\perp}/v_{e\perp}|$, $v_{e\perp}$ and $v_{h\perp}$ are, respectively, the perpendicular components of the electron and hole group velocities, and Γ_e and Γ_h are the inverse electron and hole lifetimes, respectively. This general formula can be reduced under the condition $v_h \ll v_e$ to the following:

$$\Gamma = \Gamma_h, \qquad \Gamma_h \gg \Gamma_e |v_{h\perp}/v_{e\perp}| \tag{2.12a}$$

$$\Gamma = \Gamma_e |v_{h\perp}/v_{e\perp}|, \quad \Gamma_h \ll \Gamma_e |v_{h\perp}/v_{e\perp}|. \qquad (2.12b)$$

For layered compounds or surface states, $v_{h\perp} = 0$; thus only hole lifetimes contribute to the peak broadening [35].

The photoelectron and photohole decay through different channels. Photoelectrons can create characteristic excitations of the solid (plasmons, interband transitions) which usually have an energy in the 10-20 eV range [35]. For electrons escaping from the crystal with sufficient energy to create a characteristic excitation, the inverse lifetime (or imaginary part of the self-energy) generally takes a value of about 4 eV and varies little from one material to another. The lifetime of photoholes in the valence band is usually much longer. The characteristic decay process for holes in the valence band is via the Auger mechanism, i.e., creation of electron-hole pairs. For a Fermi liquid system, holes have practically infinite lifetimes at the Fermi level due to the Pauli exclusion principle. Away from the Fermi level, from a simple phase space argument, the inverse lifetime varies quadratically with energy about the Fermi level [36-37]. Semiconductors, insulators, and superconductors below their transition temperatures have rather large lifetimes for states which are less than a band-gap energy away from the valence or conduction band edges, for these states cannot decay by creating electron-hole pairs due to the absence of any density of states within the gap. Beyond that energy range, lifetimes are comparable to metals.

2. Many-body effects

So far we have discussed photoemission processes in the framework of the one-electron model. In a real process, however, the state of the emitted electron is related to the state of the N-1 electrons remaining in the solid. Thus, photoelectron spectroscopy does not necessarily give a spectrum related simply to the initial state spectrum.

To consider the final state effects, there are two approximations corresponding to two extreme cases. One is the adiabatic approximation, which assumes that the photoelectron is removed very slowly so that the N-1 remaining electrons have enough time to adjust themselves to minimize the total energy in the new potential. In this case, the final hole is well screened, and the photoelectron has maximum kinetic energy. This approximation may be good for valence band photoelectrons with low kinetic energies. In the other extreme, if the photoelectron is removed with large velocity, the N-1 electrons remain in their original state before photoexcitation. Then the sudden approximation may be more suitable. Under this approximation, the final state should be expressed as a linear combination of the eigenstates in the new potential. As a result, the emitted photoelectron will have a distribution of energies different from that of Koopmans' theorem or the adiabatic approximation. Quite often, the additional peaks are called satellite peaks.

Generally, for a metallic system with sufficient itinerant character, the photoemission spectrum can be considered to reflect the density of initial states modulated by the single particle matrix elements, because a large number of electrons will respond to the presence of a

hole. On the other hand, if the system has pronounced localized character, such as deep core levels and 4f electrons in Ce, the simple interpretation of the photoemission spectrum in terms of density of initial states can be completely erroneous. The spectral function now has to be calculated in a many-body formalism. There are many successful efforts in this direction for the 3d transition metal oxides and 4f light rare earth systems [38-39]. Some of the methods were also applied to high T_c superconductors [40].

III. EXPERIMENTAL DETAILS

A. Light Source and Beamline

The photons are provided by the Aladdin storage ring [41] at Synchrotron Radiation Center, in Stoughton, Wisconsin. The storage ring operates at 800 MeV, and produces photons in the ultraviolet and soft X-ray energy range. The measurements are made on the Ames/Montana ERG/Seya combined monochromator beamline. The beamline is designed by C. G. Olson [42]. Figure 4 is its schematic layout. The beamline covers the energy range 5 eV to 1 keV. The ERG is for high energies, and the Seya is for low. Photons coming out of the beamline are almost completely polarized. The Seya has four gratings with different ruling densities. Their output characteristics are shown in Fig. 5. The Seya 1800 l/mm grating was used in the experiments described in this thesis.

The energy resolution of the monochromator is determined by the slit width, the grating ruling density, the grating radius, and the photon energy. For the Seya, at a slit width of 200 μm, the slit accepts all of the beam from Aladdin. Because of the use of a spherical grating and a straight slit, the line shape has a tail to the long wavelength side. As a result, the monochromator instrument function is a skewed Gaussian, and the FWHM is larger than it would be in an ideal case. For example, for 22 eV photons, the FWHM is 24 meV.
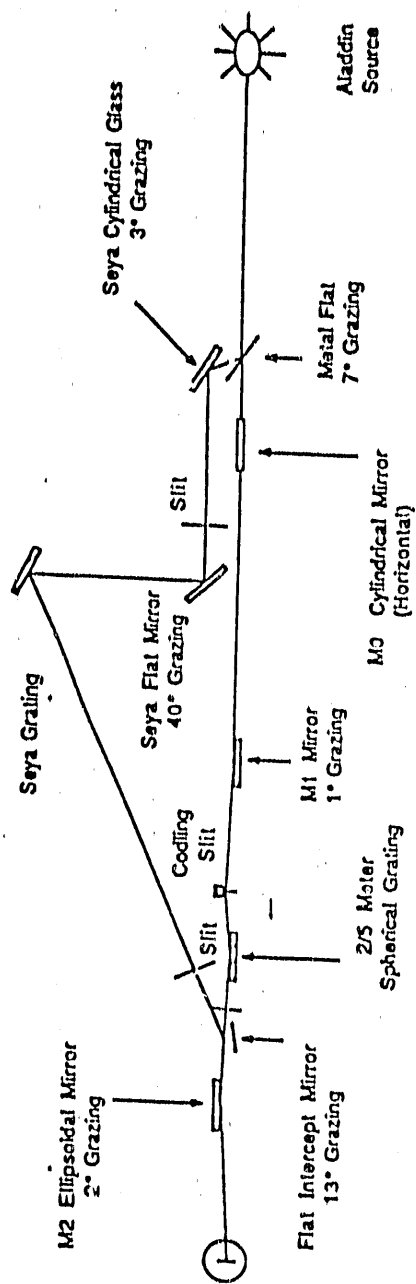
Fig. 4. Schematic layout of the Ames/Montana ERG/Seya combined monochromator beamline
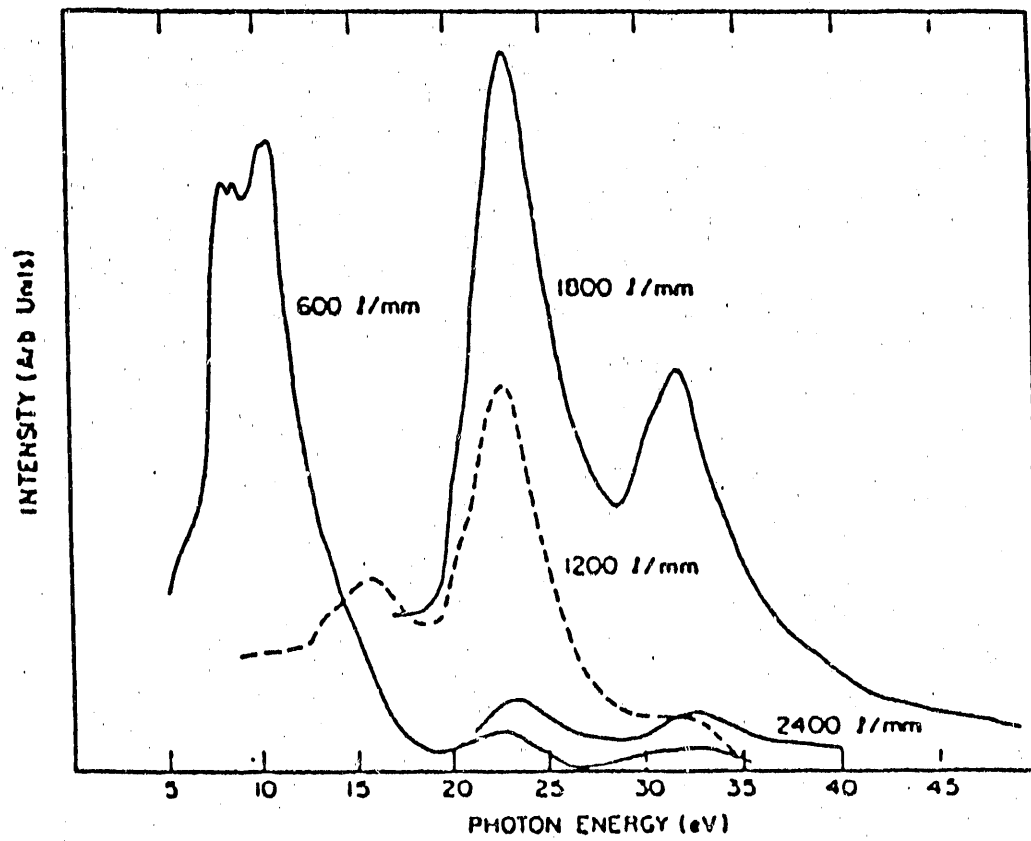
Fig. 5. Spectral output of the Seya

B. Electron Energy Analyzer

A VSW (Vacuum Science Workshop) hemispherical electron energy analyzer [43] was used for collecting and analyzing the emitted photoelectrons. The analyzer is mounted on a goniometer which has two degrees of rotational freedom. Figure 6 is a schematic presentation of the analyzer. Basically, it is composed of a 1:1 retarding lens in the front, the hemispherical deflectors as the dispersing element, and a channeltron which collects and amplifies the signal. Some of the details in design were modified and improved by C. G. Olson.

The analyzer has an angular acceptance of 2°. The k-space resolution is determined by both the angular acceptance and the photoelectron kinetic energy. For a certain emission angle and kinetic energy, the parallel wave vector is determined by the relation $k_{||} = (2mE_K/\hbar)^{1/2} sin\theta$. For example, if the photon energy is 22 eV, E_K would be about 16.5 eV. Then, the 2° angular resolution corresponds to a k resolution of 0.075 Å^{-1}. Compared to the dimension of the Brillouin zone of $Bi_2Sr_2CaCu_2O_8$, which is about 1.16 Å^{-1}, this angular resolution is sufficient for band mapping.

The energy resolution of the analyzer is given approximately by:

$$\Delta E = E_p(d/2R + \alpha^2/4),$$

where E_p is the pass energy, d is the slit width, R is the mean radius of the hemispheres, and α is the full angle of electrons entering the analyzer. Usually, α is only a few degrees, and the second term can be neglected. For our analyzer, $d = 1$ mm, $R = 50$ mm. Thus, the
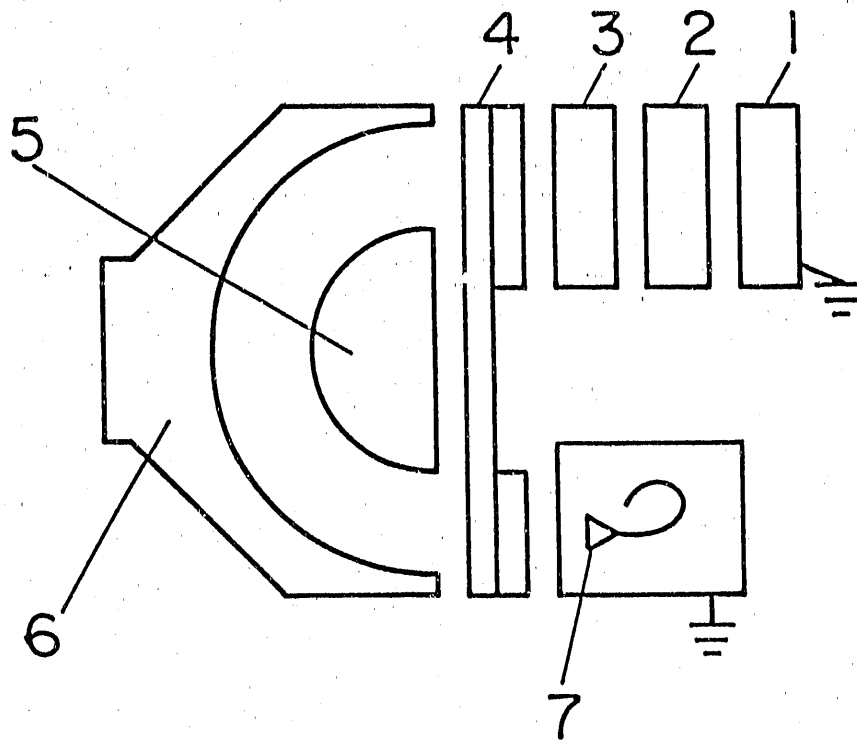
Fig. 6. Schematic configuration of the VSW HA50 hemispherical electron energy analyzer. 1-4: entrance lens; 5,6: hemisphere deflectors; 7: channeltron

energy width is about 1% of the pass energy. For example, the energy resolution is about 20 meV for a pass energy of 2 eV.

In most of the experiments described in this thesis, 2 eV pass energy and 22 eV photon energy were used. In analyzing the data, we used a tabulated instrument function, which was obtained by convolving the measured monochromator function with a 20 meV FWHM Gaussian. The resultant function is a skewed Gaussian with an asymmetric tail at the low binding energy side, as shown in Fig. 7. The FWHM is about 32 meV.

C. Vacuum Chamber and Sample Preparation

The experiments were made in a vacuum of better than 5×10^{-11} Torr. Inside the vacuum chamber, there is a double layer of μ-metal for shielding the earth's magnetic field. A chamber with a very low field is important for high-resolution valence band studies, since a pass energy as low as possible would be desired. The chamber is equipped with an ion sputtering gun which was used for cleaning the Pt foil for Fermi level reference.

The single crystals of $Bi_2Sr_2CaCu_2O_8$ were grown at Argonne National Laboratory. They had typical dimensions of 2mm $\times$ 2mm $\times$ 0.1mm. Their transition temperatures are about 82K, determined from magnetic susceptibility measurements. The samples were mounted with Torr-Seal epoxy to the end of a 2mm diam. $\times$ 8mm long Al rod, which was in intimate contact with the cold finger of a closed cycle He refrigerator. A second Al rod was then mounted on top of the samples. Electrical contact was established via a coating of
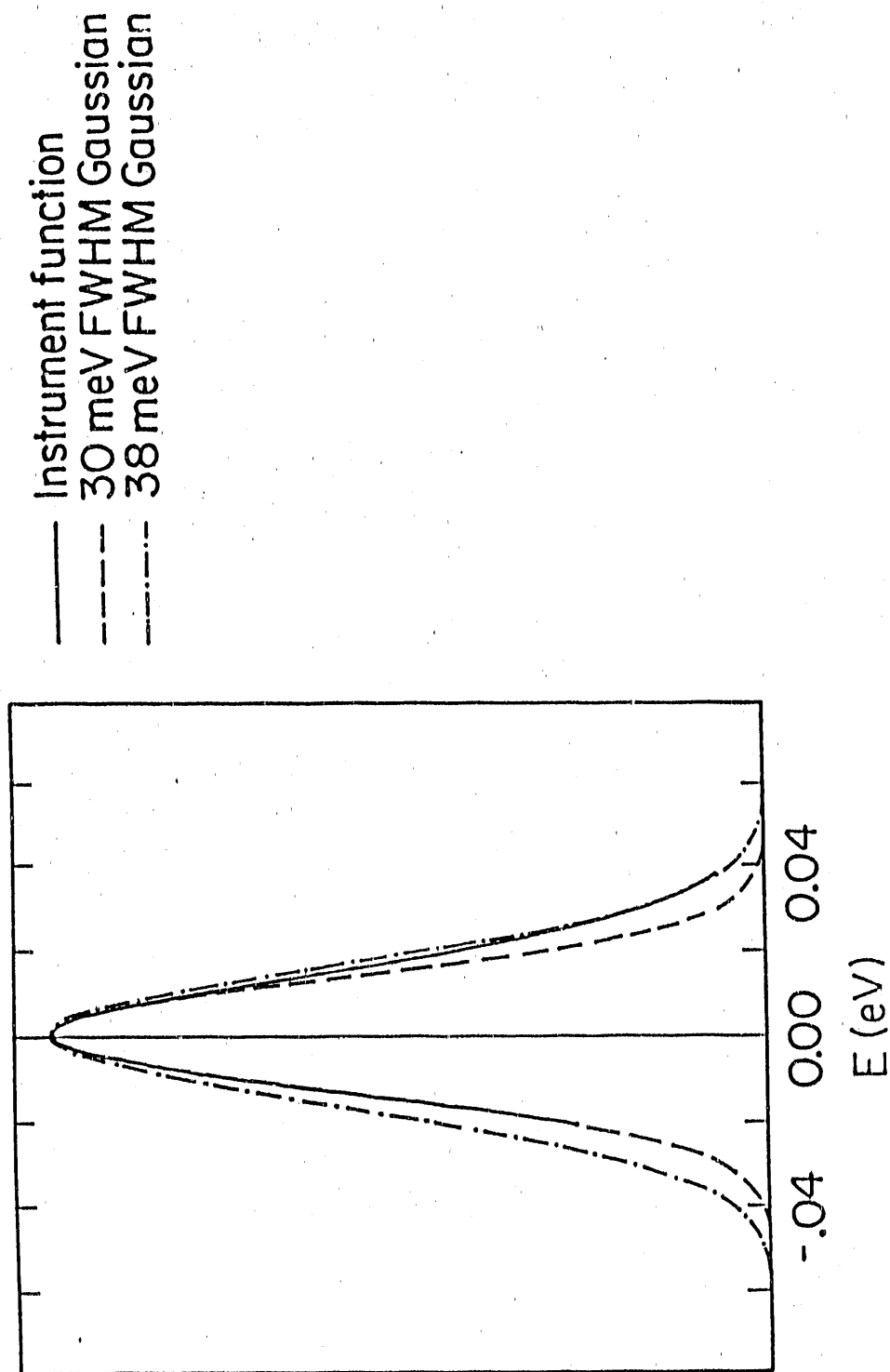
Fig. 7. The intrument function of our spectrometer (solid line), when 2 eV pass energy and 22 eV photons are used. A 30 meV (dashed line) and a 38 meV (dot-dashed line) FWHM Gaussian function are shown for comparison

Instrument function
30 meV FWHM Gaussian
38 meV FWHM Gaussian

-.04   0.00   0.04

E (eV)

aqua-dag bridging the epoxy. The samples were cleaved by prying on the top Al rod in situ at 20K. The surfaces were (001) planes. The samples were oriented by Laue X-ray diffraction before mounting in the chamber.

IV. RESULTS AND DISCUSSION

A. Normal State

1. Introduction

Since the discovery of high T_c superconductors, their electronic structures have been of great interest. Whether or not the normal states of these materials are Fermi liquids has been a key question. Is one-electron band theory adequate as a starting point for describing the normal-state electronic structure (with added modifications from correlation effects) or must an alternative description be devised [16, 17]? Answers to these questions are important for the ultimate understanding of the mechanism of superconductivity in these materials.

In an attempt to address some of these questions, we carried out a detailed angle-resolved photoemission study on normal-state $Bi_2Sr_2CaCu_2O_8$. The experiment was performed with high energy and angular resolution, a prerequisite for studying the details of the states near the Fermi level. To minimize thermal broadening, measurements were made at temperatures just above T_c.

An angle-resolved photoemission study on high T_c superconductors is simplified by the fact that most of the structures are highly two-dimensional. In the photoemission process, momentum parallel to the surface is conserved. Momentum perpendicular to the surface is not conserved since the photoelectron transfers a certain perpendicular momentum to the crystal when escaping through the surface barrier. For a two-dimensional system, however, the momentum parallel to the

surface is sufficient to determine the initial state.

By measuring photoelectron energy distribution curves (EDCs) at 90K (above T_c) as a function of angle, we were able to isolate a single band dispersing through the Fermi level, and determine the point in the Brillouin zone where the band crosses the Fermi level. The measurement is accurate to 2°. (For 22 eV photon energy, this corresponds to $\Delta k_{\parallel} = 0.075 Å^{-1}$.) Such measurements were made along major symmetry lines. The basic features of the Fermi surface were obtained. The results will be presented and discussed in three sections: band dispersion and the Fermi surface, a more detailed analysis of the spectral line shapes, and a comparison of the filled states at the Fermi level to a conventional Fermi liquid.

2. Band dispersion and Fermi surface

Before we discuss the photoemission data, let us first look at the crystal structure of $Bi_2Sr_2CaCu_2O_8$. Similar to La_2CuO_4 and $YBa_2Cu_3O_7$ high T_c superconductors, $Bi_2Sr_2CaCu_2O_8$ has a layered perovskite-like structure as shown in Fig. 8 [44, 45]. The unit cell consists of two CuO_2 layers separated by a Ca layer, and rock-salt type Bi_2O_2 layers. The $(CuO_2)Ca(CuO_2)$ layers are separated by single SrO layers from Bi_2O_2 layers. The structure is face-centered orthorhombic (but quasi-tetragonal), with lattice parameters $a = 5.414$ Å, $b = 5.418$ Å, $c = 30.89$ Å. The actual crystal structure may be more complicated. $Bi_2Sr_2CaCu_2O_8$ is known to have a superlattice structure along the b-axis with an effective lattice constant 25.8 Å [45, 46]. The exact cause of the formation of this superlattice

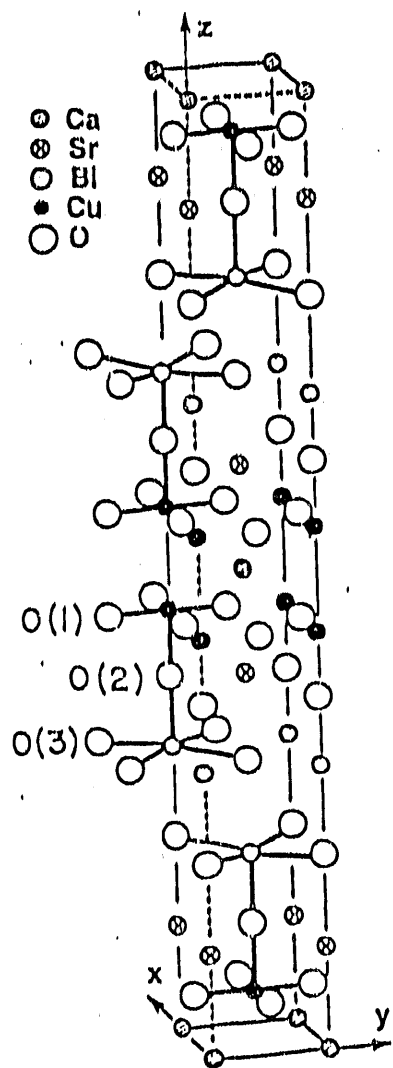Fig. 8. Idealized crystal structure of $Bi_2Sr_2CaCu_2O_8$ (Ref. 44)

is not known. It is suggested that the mismatch of Bi-O ionic radii to the Cu-O layer cell is a possible cause [47]. Most of the band calculations were performed using the parent crystal structure.

Several band calculations exist [48-50]. They all produce more or less similar features. Shown in Fig. 9 is the band structure of $Bi_2Sr_2CaCu_2O_8$ along major symmetry lines in the Brillouin zone calculated by Massidda et al. [48]. First, we note that bands disperse very little from Γ to Z, implying a highly two-dimensional electronic structure. Above a set of fully occupied bands (48 bands, mostly consisting of Cu d and O p character), only three highly dispersive bands cross the Fermi level. Along $\Gamma - X$ and $\Gamma - Y$, two nearly degenerate bands with Cu-O pdσ character cross E_F, forming hole Fermi surfaces centered at X and Y. Along $\Gamma - \overline{M}$ a band with Bi-O ppσ character dips below E_F, forming an electron Fermi surface centered at $\overline{M}$. The Fermi surface calculated by Massidda et al. [48] in the extended Brillouin zone is shown in Fig. 10. The shaded region has hybridized Cu-O and Bi-O character. There are suggestions that the Bi-O layers play the role of an electron reservoir and have the effect of self-doping the Cu-O layers [51]. However, whether the Bi-O band crosses the Fermi level is questioned and doubted by many people.

The spectra in Fig. 11 are taken in normal emission. In this geometry a shift in the binding energy of a peak as a function of photon energy represents dispersion along the direction normal to the surface, which is the a-b plane. As can be seen in Fig. 11, there is minimal dispersion. The primary effects are a small shift of the 3.5 eV peak to lower binding energy with increasing photon energy and a larger shift of the 4.8 eV peak to higher binding energy. The small amount

31
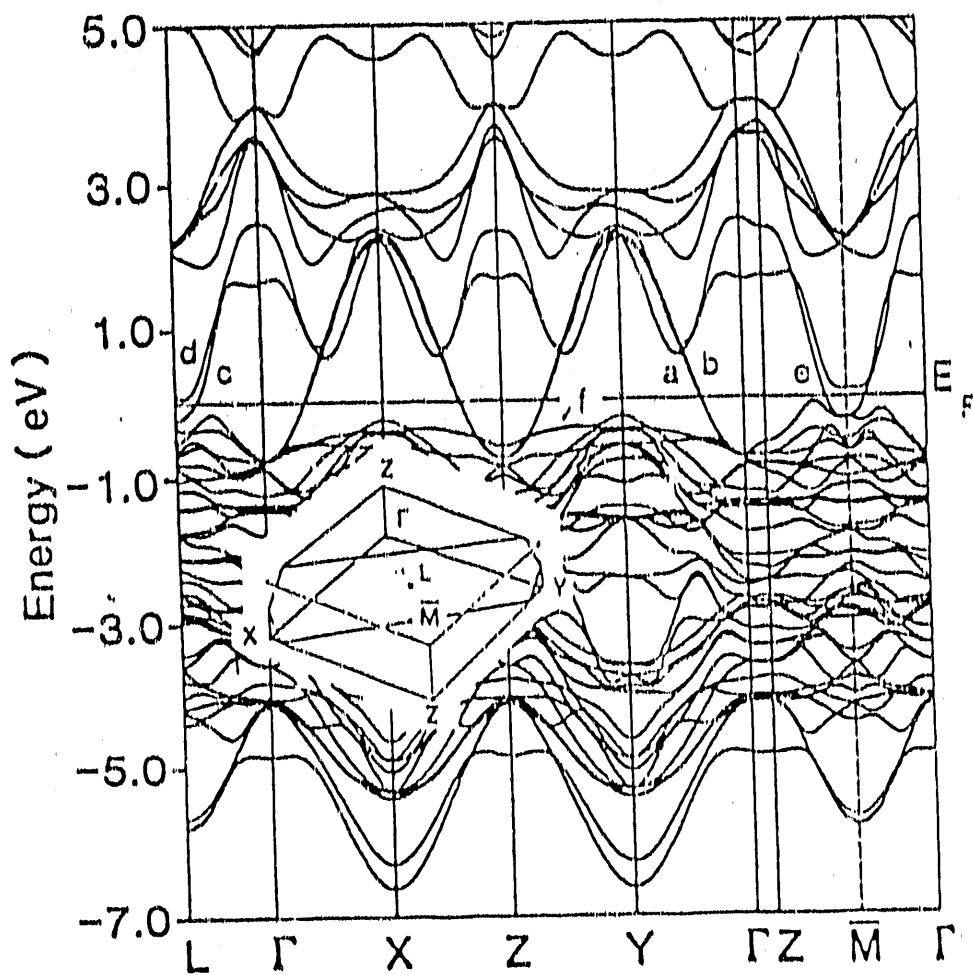

Fig. 9. Energy bands of $Bi_2Sr_2CaCu_2O_8$ along the main symmetry lines of the face-centered orthorhombic Brillouin zone shown as insert (Ref. 48)

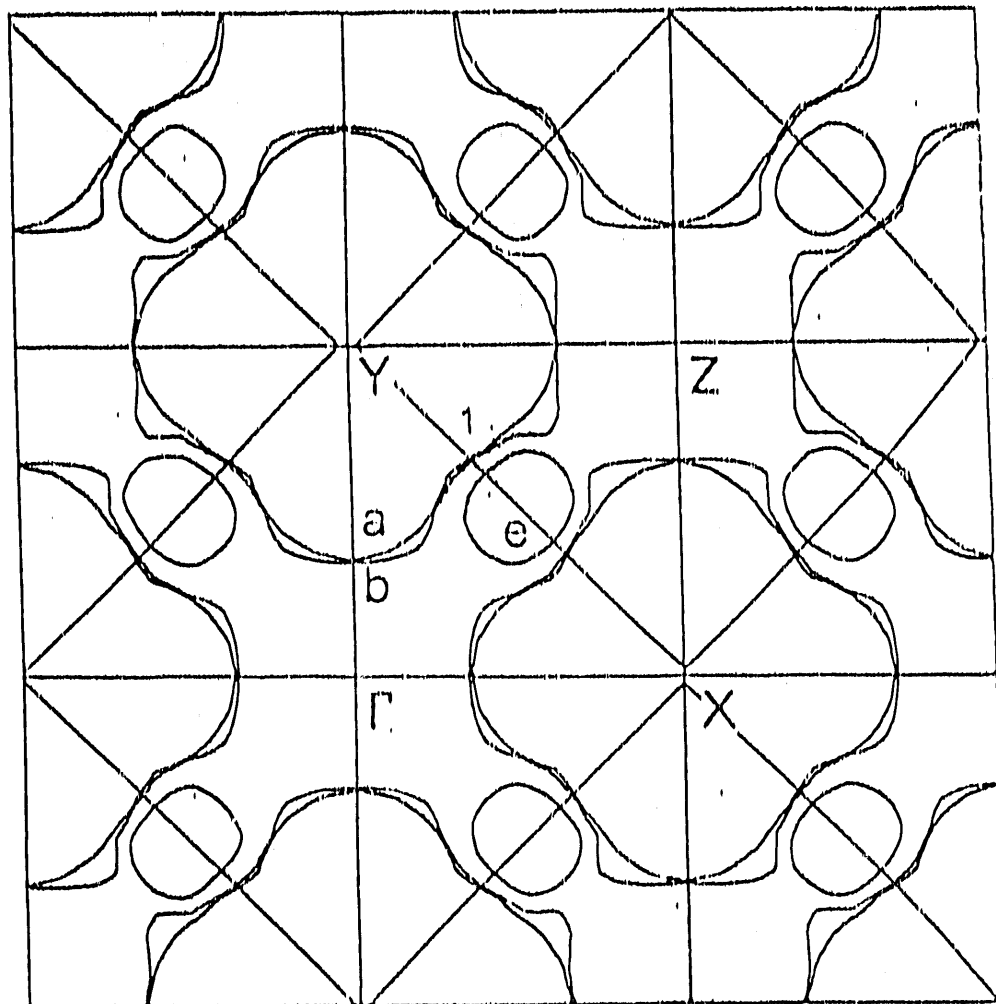Fig. 10. Fermi surfaces of $Bi_2Sr_2CaCu_2O_8$ in an extended zone scheme (Ref. 48)
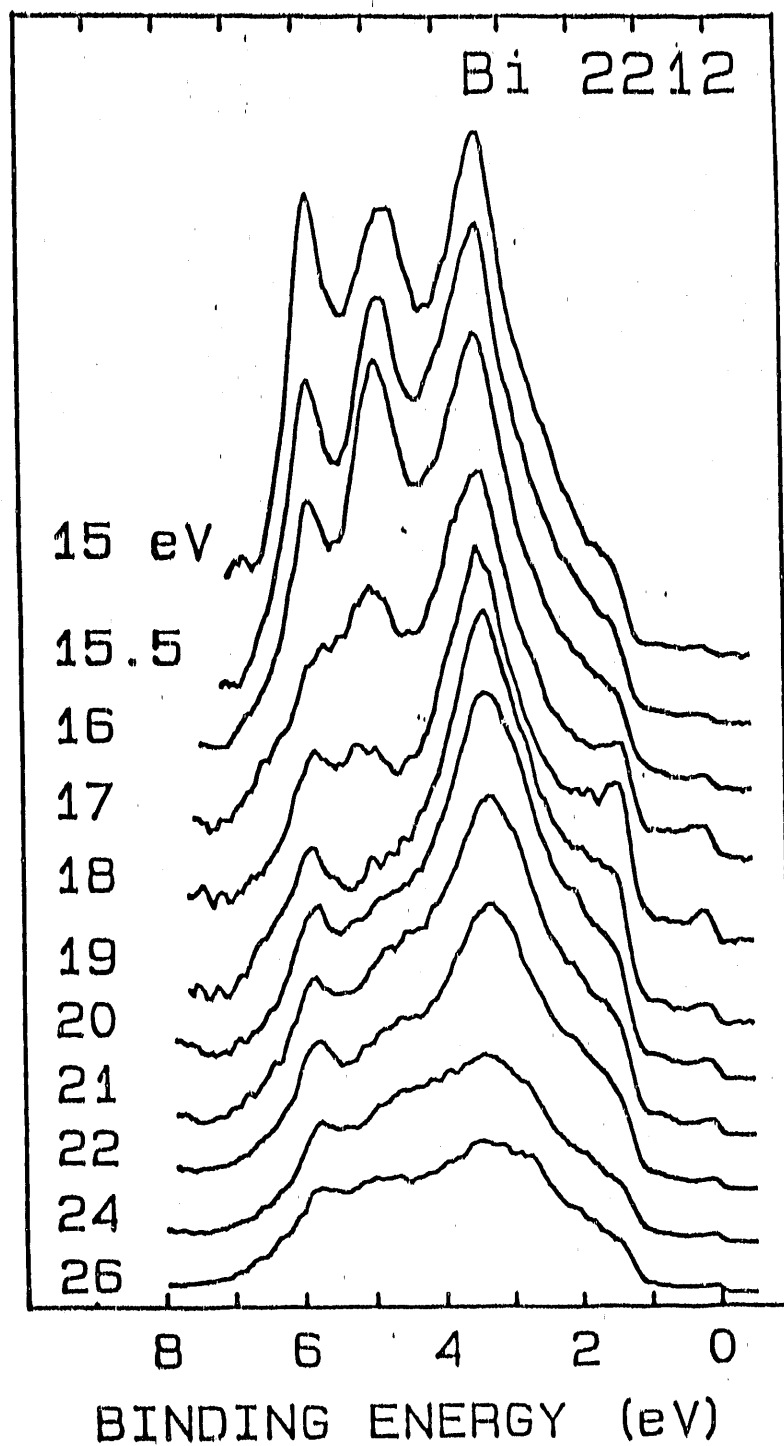
Fig. 11. Photoemission energy distribution curves taken in normal emission for $Bi_2Sr_2CaCu_2O_8$

of dispersion in the $\Gamma - Z$ direction is not surprising in this highly two-dimensional material and is consistent with the band calculation [48]. Dispersion in less well-defined peaks is masked by the very strong intensity modulations due to matrix element effects. The enhancement near the Fermi level and at 1.5 eV for photon energies near 18 eV is a manifestation of the strong selection rule effects.

The spectra shown in Fig. 12 are taken at 90K along a line parallel to $\Gamma - Y$ (the k points in the Brillouin zone corresponding to the zero binding energy of each spectrum are shown as solid dots in Fig. 13). It can be seen that a band disperses toward the Fermi level from at least 350 meV below E_F. At 12°, the Lorentzian peak is cut off by the Fermi-Dirac function, and the leading edge coincides with the Pt edge. This is a clear indication that the band has just crossed the Fermi level at this point. As indicated in Fig. 13, the 12° point almost falls on the Fermi surface predicted by band calculations [48]. At 14°, the band has completely passed the Fermi level. The details of the spectral shapes will be discussed in the next section.

The dispersion of this band is shown as the insert of Fig. 12. The band is less steep and the minimum at Γ is closer to E_F than predicted by a one-electron band calculation [48]. It agrees better with the band structure of a "heavy Fermion" state calculated within the formalism of the Anderson lattice model with a large Coulomb interaction U taken into account [52]. The effective mass of this band is estimated to be 2 from our experimental data. A similar increase in mass above the calculated mass was observed by Manzke et al. [53].

One of the tests of the band calculations is whether a band calculated to have Bi-O character crosses the Fermi level, i.e., whether

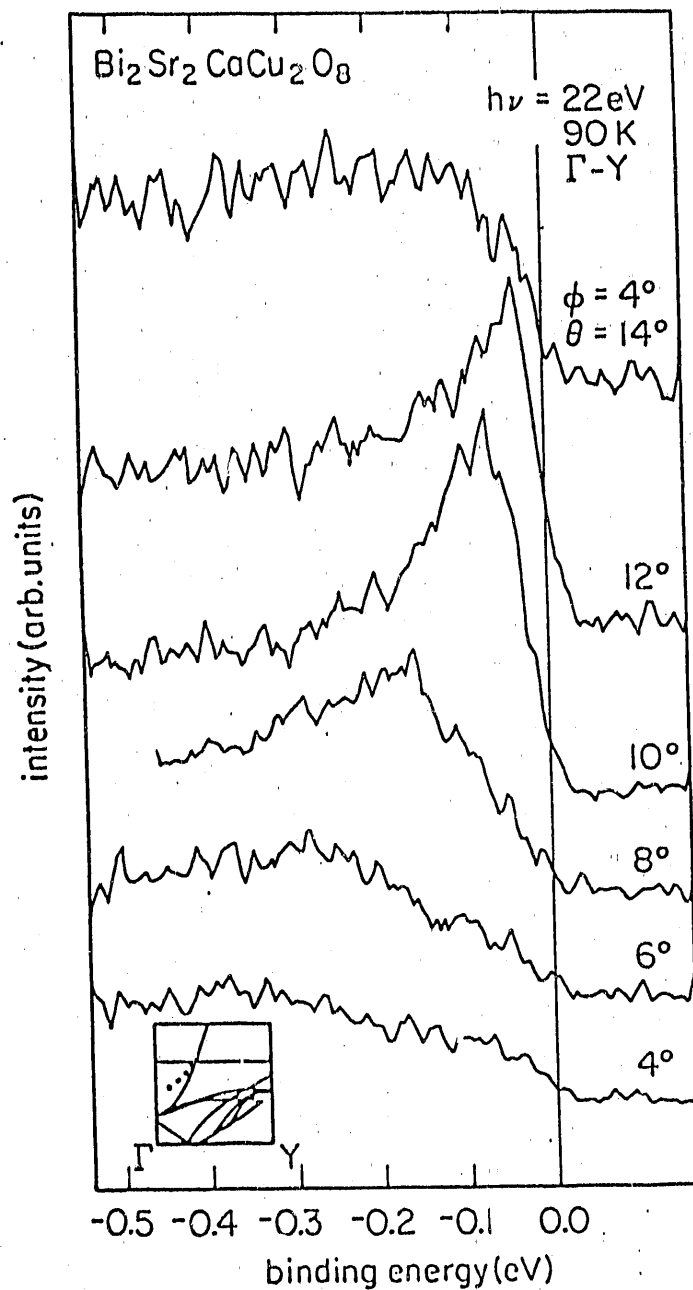Fig. 12. Angle-resolved energy distribution curves for several angles along the $\Gamma - Y$ direction in the Brillouin zone using photons of energy 22 eV. The inset shows the measured band dispersion (dots) and the calculated bands from Ref. 48
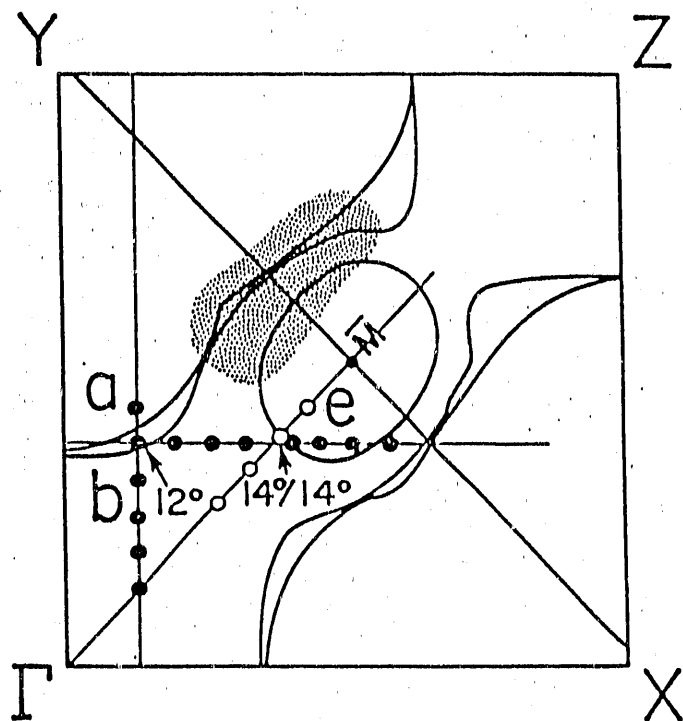
Fig. 13. Section of the calculated Fermi surface of $Bi_2Sr_2CaCu_2O_8$ (from Ref. 48) showing points at which bands crossing the Fermi level were observed

the circular shaped Fermi surface labelled e by Massidda et al. [48] in Fig. 13 exists. To investigate this, we measured EDCs along $\Gamma - \overline{M}$. The spectra are shown in Fig. 14. (The k points in the Brillouin zone corresponding to zero binding energy of each spectrum are shown as open circles in Fig. 13.) It can be seen that a rather flat band disperses towards the Fermi level, and at 14° the band crosses the Fermi level. As indicated in Fig. 13, this point is exactly on the intersection of $\Gamma - \overline{M}$ and the circle e. Therefore, it is quite certain that this piece of Fermi surface does exist, although we cannot prove that this part of the Fermi surface has some Bi character, since there is no good Bi resonance that we can use. We note that the measured band is closer to E_F than predicted by Massidda et al. [48]. With that adjustment the enhancement of the effective mass is similar to that of the Cu-O band studied in Fig. 12. However, the band near E_F is more complex than the nearly parabolic Cu-O band. An estimate of the effective mass in that region is difficult.

Fig. 15 shows a series of EDCs taken at 90K along a line parallel to $\Gamma - X$ (Fig. 13). Along this line, the density of states near the Fermi level is always quite high. However, if we look more closely, we find that the density of states at the Fermi level decreases on going from $\phi = 4°$ to 6° to 8°, indicating the departure of the band from the Fermi level. At 10° and above, the density of states at the Fermi level increases again. Shown in Fig. 16 is another set of scans taken at 20K in the direction parallel to the scan of Fig. 15. With the gap pile-up (see Section B.1), it is hard to keep track of the dispersion. From Fig. 15 and Fig. 16, we see filled states near the Fermi level throughout much of this part of zone. With our resolution it is not possible

Fig. 14. Angle-resolved energy distribution curves for several angles along the $\Gamma - \overline{M}$ direction in the Brillouin zone using photons of energy 19 eV. The inset shows the measured band dispersion (dots) and the calculated energy bands of Ref. 48
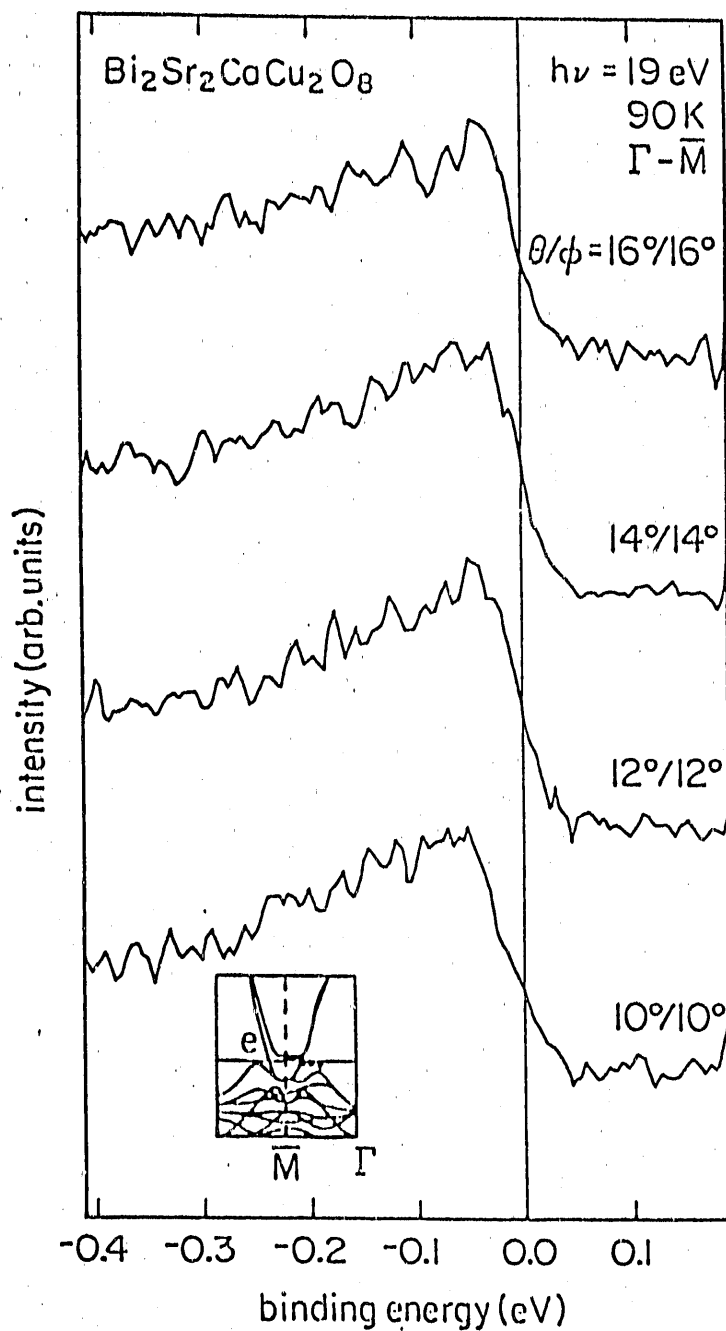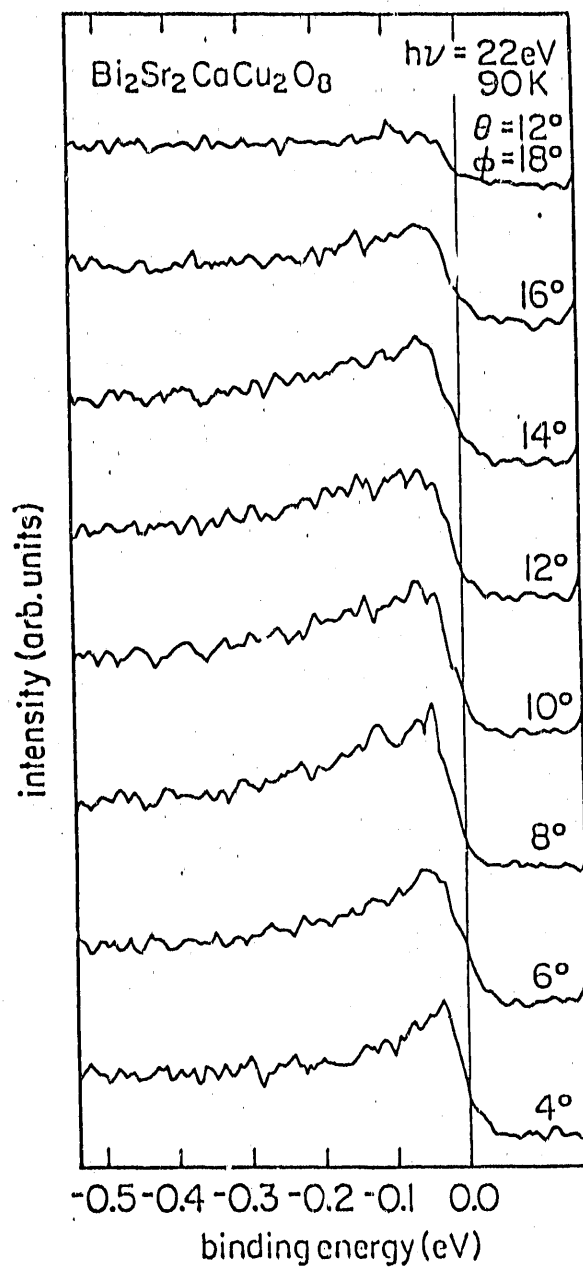
Fig. 15. Angle-resolved energy distribution curves for several angles along a line parallel to $\Gamma - X$ in the Brillouin zone using photons of energy 22 eV
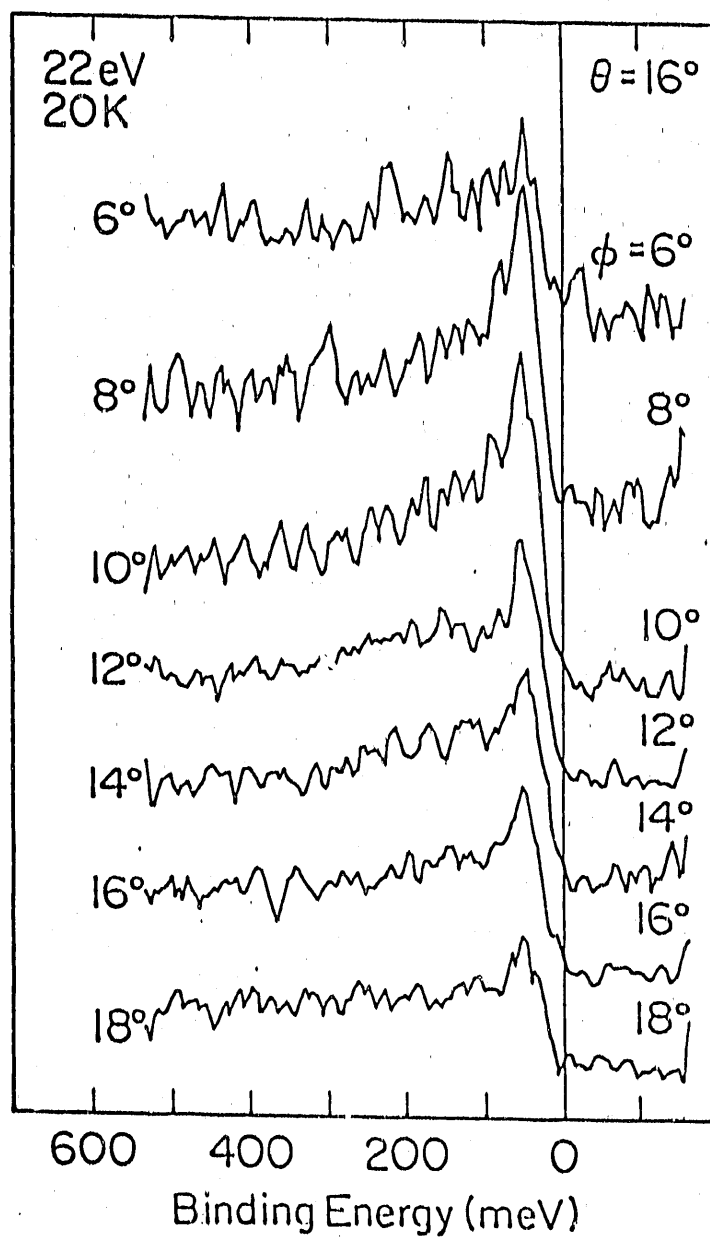
Fig. 16. Angle-resolved energy distribution curves at 20K for several angles along a line parallel to the direction of Fig. 15 using photons of energy 22 eV

to show whether the Fermi surface section centered on $\overline{M}$ is or is not connected to the sections centered on X or Y, and whether the band through this region has its minimum at Γ or $\overline{M}$. However, the Fermi surface crossing is consistent with Fig. 13.

Since the structure of $Bi_2Sr_2CaCu_2O_8$ is quasi-tetragonal, we would expect similar band dispersion along $\Gamma - X$ and $\Gamma - Y$. The corresponding band was seen along $\Gamma - X$, but it was necessary to use 19 eV photons. The photon beam is almost completely polarized, and selection rules and electric dipole matrix element effects are dramatic. A second crystal was mounted rotated 90° about the c-axis from the first. This time the $\Gamma - X$ band was easily seen at 22 eV, but not at 19 eV, verifying the dipole matrix elements as the cause of the anisotropy. This also shows that the superlattice plays no role.

To summarize, we have observed band dispersion along major symmetry lines and the main features of the Fermi surface are obtained. The agreement between the experiment and the band calculations of the Fermi surface is surprisingly good. The existence of a Fermi surface, the large band dispersion with effective masses enhanced by correlation effects, and the strong dipole matrix element effects all strongly support a Fermi liquid description of this material.

The facts that the one-electron band calculation is successful in predicting the Fermi surface, but failed to give an accurate band dispersion, are not contradictory. If this system is a true Fermi liquid, Luttinger's theorem [54] should be obeyed, which means the Fermi volume is invariant under interaction effects. Therefore, unless there is a strong anisotropic potential, the Fermi surface should be preserved.

3. Photohole lifetime

The peak widths and line shapes of the spectra in Fig. 12 need more attention. Generally the peak widths are determined by the inverse lifetime of both photoelectrons and holes, in addition to the contributions from instrument resolution. However, for a two-dimensional system, only the hole lifetime contributes to the broadening; the lifetime of the emitted electron does not broaden the peak [35-55]. Holes at the Fermi level have practically infinite lifetimes. Away from the Fermi level, for a normal Fermi liquid, the inverse hole lifetime increases as $(E - E_F)^2$ in all dimensions. There are other possibilities. Recently, a linear dependence on $|E - E_F|$ has been suggested for a "near" Fermi liquid model [56], and Fermi surface nesting has been shown to predict such a dependence [57]. Finally, another model exists which accounts for many of the features of our data: dispersion of peaks in the EDCs and the widths of these peaks [58]. The modified single particle band structure has been successful in describing the data to this point, however, and we will discuss Fig. 12 in this context.

A discussion of the broadening in Fig. 12 is complicated by the finite angular resolution. For the 10° spectrum, the peak width is determined by our k resolution. (The energy broadening caused by k resolution at this k point is about 84 meV, using the equation $\Delta E = (dE/dk)\Delta k$. dE/dk is estimated from the experimental data.) For the 12° spectrum the measured peak is narrower because only part of the sampled band is filled. As the band moves below the Fermi level, the width increases rapidly. Below 350 meV, the peak became

too broad to be distinguished from the background. The asymmetry of the peak is another consequence of the finite angular resolution. There is a significant change in photohole lifetime from one side of our angular acceptance to the other.

We modelled this effect by assuming the angular acceptance function was a square function. Its 2° full width was converted to a width in $k_\parallel$, then to a width in energy via the measured dispersion of the band. The spectrum was simulated by a series of 200 equally spaced Lorentzians throughout the corresponding energy range each with a width of $\alpha|E - E_F|$ or $\beta(E - E_F)^2$. These were summed, then multiplied by the Fermi function and convoluted with the part of the instrument resolution not arising from the finite angular acceptance. For any single spectrum, a value of α and β could be found that gave a fit. However, upon going to other angles and repeating the analysis with the same values of α and β, the quadratic energy dependence of the width gave EDCs that were much more asymmetric than the measured ones, while the linear energy dependence gave a good fit. The best value of α was 0.6 (dimensionless). Replacing the rectangular angle resolution function by a Gaussian gave essentially the same results. The effectively linear dependence of inverse photohole lifetime on energy is consistent with the predictions of Refs. 17 and 18. It should be pointed out that not only the energy dependence of the inverse hole lifetime is different from Fermi liquids, its magnitude is also significantly larger, as illustrated in Fig. 17.

The resulting fits, using a linear energy dependent broadening are shown in Fig. 18. The data are from Fig. 12 with a background removed. The background at a given binding energy was taken to be
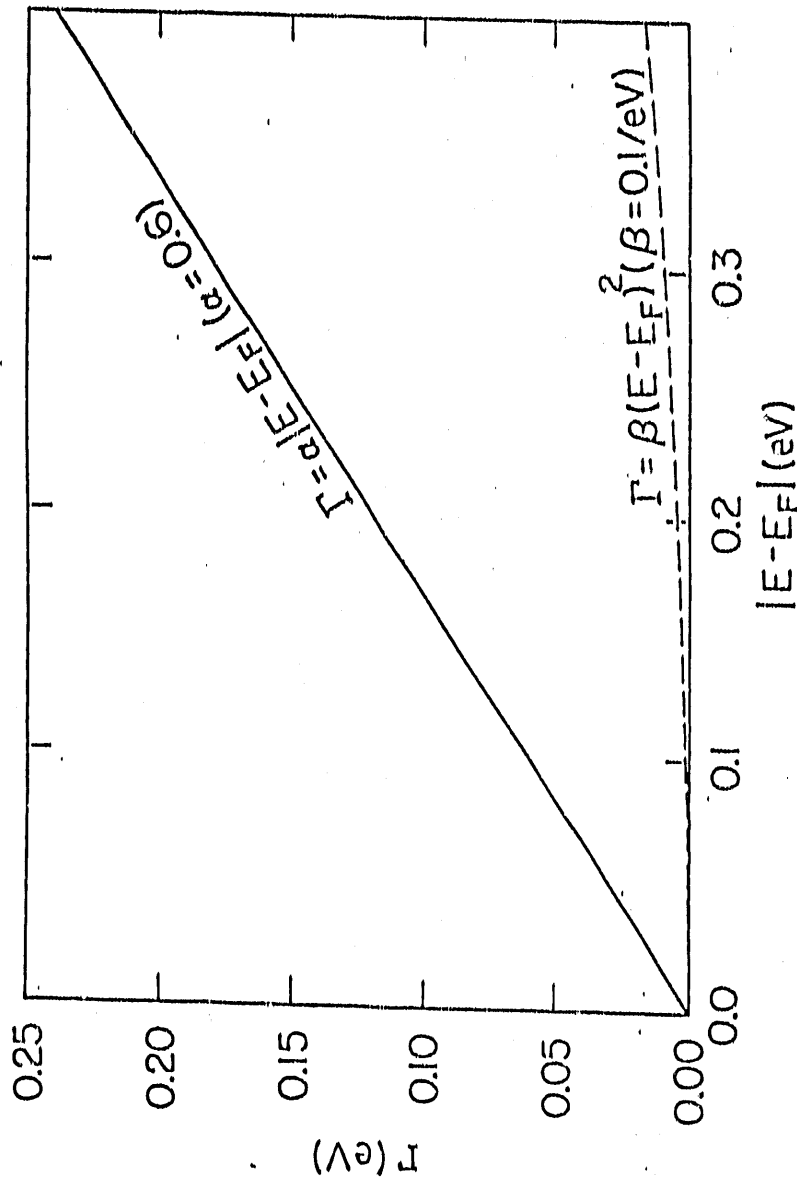
Fig. 17. Comparison of the inverse photohole lifetime of $Bi_2Sr_2CaCu_2O_8$ (linear function, solid line) and that of Fermi liquids (quadratic function, dashed line). The co-efficient α is obtained from the fitting as described in the text. A typical value of β in ordinary transition metal is used

Fig. 18. Spectra of Fig. 12 with a background removed. The lines are the fits using a linear energy dependent broadening as described in the text

proportional to the sum of the primaries at higher kinetic energies. The same constant was used for all spectra. The success of this background method implies that there is a difference between primary and secondary electrons of the same kinetic energy. There is a consistent physical picture in this case if the background is composed of primary electrons that have suffer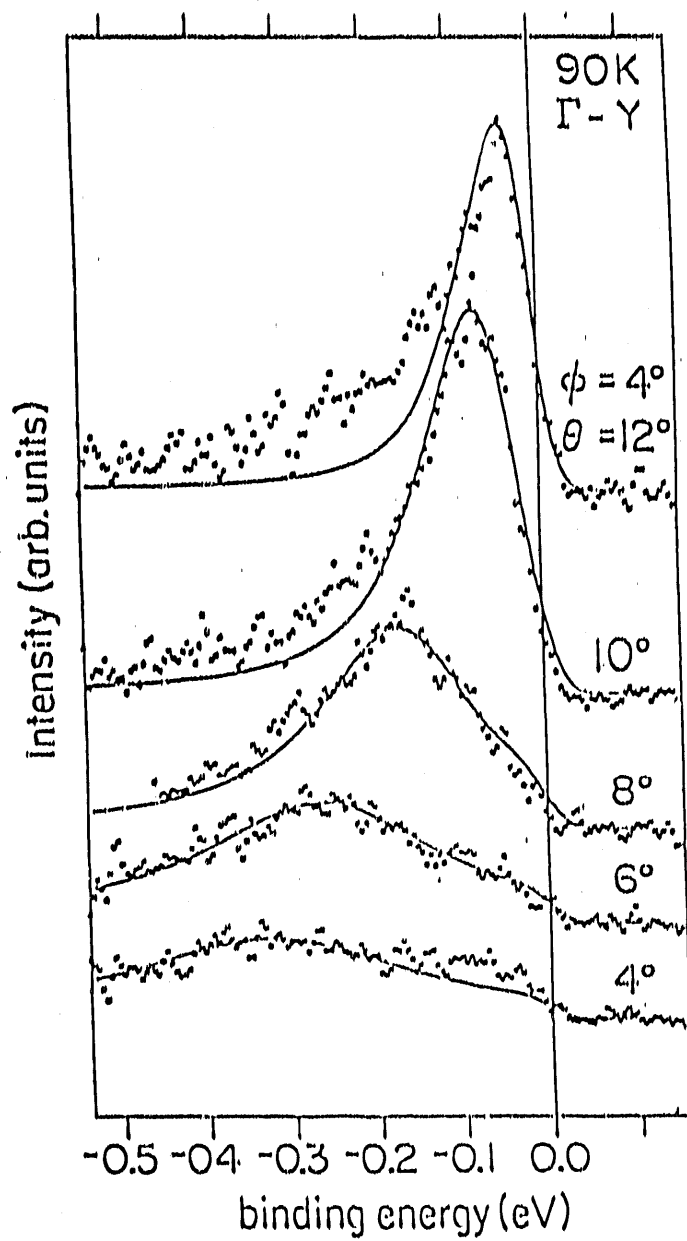ed a small energy loss and small change in momentum at or near the surface. It is very unlikely that electrons with multiple losses will appear in the energy window of these spectra, and the conventional secondary electrons appear at much lower kinetic energies.

The background determined by this method for the 12° spectrum in Fig. 12 is exactly the measured 14° spectrum. There are no filled states at E_F for the momentum corresponding to 14° within the angular acceptance at our analyzer. The photoelectrons we detect have been scattered into the analyzer acceptance with small changes in momentum and small energy loss. Hence there is no emission at E_F (the highest kinetic energy), and the scattered electron spectra are equivalent over a small range of angles. In general points in the zone there are no filled states at E_F and the background is much lower. For example this background term contributes very little to the 4° spectrum of Fig. 12 (see also Fig. 3 of Ref. 59). On the other hand, the backgrounds are universally high for the spectra in Fig. 15. Throughout this part of the zone, there are occupied states at or near the Fermi level. Scattering events with small energy and momentum changes result in a sizeable, almost energy-independent background. These are probably electron-phonon scattering events, rather than the electron-electron scattering events that appear at greater energy loss. We are

left with a picture in which the spectra are a result of conventional band dispersion through the Fermi level.

4. Temperature dependence of the Fermi edge above T_c

To examine more closely the nature of the states at the Fermi level, an EDC was measured at a point in the Brillouin zone where a band crossed the Fermi level. This point was along the line $\Gamma - \overline{M}$, and was in a region where the one-electron band calculation predicts that these electrons are mixed O 2p and Bi 6p in character [48]. Then an EDC was taken at the Fermi edge of a clean Pt foil adjacent to the sample. Such spectra taken at several temperatures between 100 and 250K are shown in Fig. 19, after suitable normalization. The stability of the observed Fermi energy in Pt for scans taken over several days was about 5 meV.

It is clear that the Fermi edges of the two materials agree at all temperatures shown. We see that the apparent Fermi energies are the same within the 5 meV stability of our electron spectrometer. This is the expectation if the material is a Fermi liquid. The resonating valence bond (RVB) [16] model prediction may be different. To explore this question, Huber [60] has made a number of simplifying assumptions, the most important of which is that instead of a photohole, a photoemission event results in the creation of a spinon and a holon which are uncoupled (or very weakly coupled). They share the energy the photohole would have. The results of Huber's calculation is that above T_c there is an edge resembling a Fermi edge. As the temperature increases, the slope of the edge diminishes while the threshold
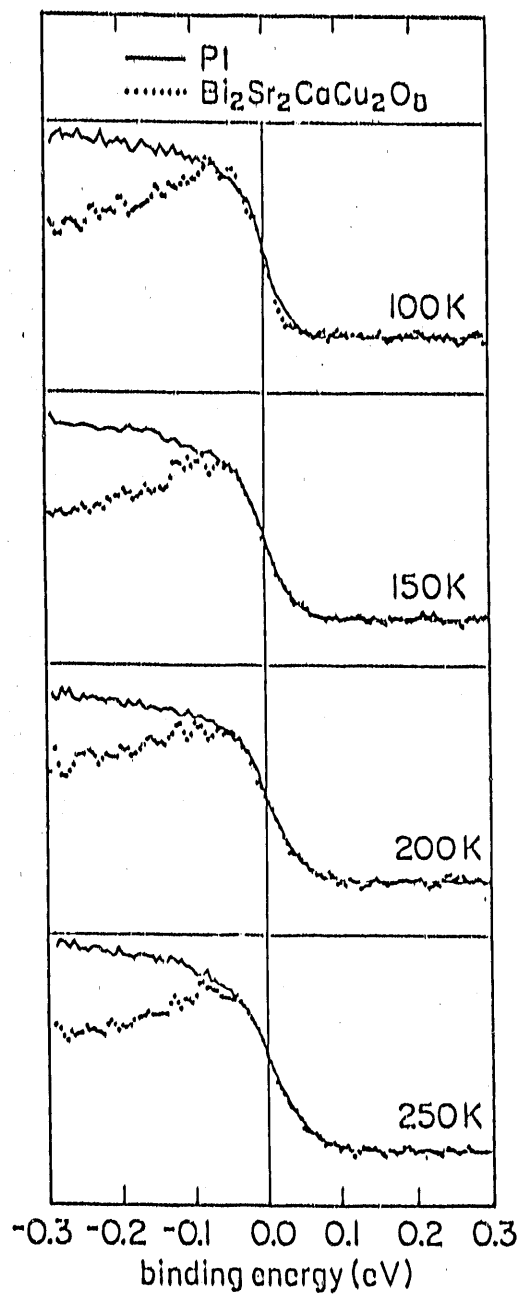
Fig. 19. Comparison of the Fermi edge of Pt with that of
Bi$_2$Sr$_2$CaCu$_2$O$_8$ at several temperatures between 100K and
250K. The plots have been normalized vertically, but not
shifted horizontally

shifts but little [61]. The effect is that the midpoint which might be identified with an apparent Fermi level shifts to lower energies. This effect is large if the maximum spinon energy is large. Thus, if the shift of the apparent Fermi energy with temperature is small, the maximum spinon energy is small. The upper bound on the shift is 5 meV.

One should note that Huber's calculation is of the density of states or spectral density in energy for an isotropic material, while our experiment samples only a small region of reciprocal space, i.e., our EDC is effectively a density of states in k-space. However, we have looked at several other points in the Brillouin zone at 90K, points with different atomic character, and see no shift of the apparent Fermi energy when compared with that of Pt, again with an uncertainty of about 5 meV.

In the strong-coupling limit the holon-spinon pair would resemble a quasielectron, and the edge should look like that expected for the Fermi-Dirac distribution function. No calculations of photoemission spectra exist for intermediate coupling strength, but any such calculations are constrained by experiment to resemble closely the Fermi liquid picture.

5. Conclusions

In conclusion, we see occupied states at the Fermi level in a relatively small area of the Brillouin zone. These areas are consistent with the calculated Fermi surface. In the normal state, this occupied density is indistinguishable from a normal metal. Away from the Fermi level, bands are heavier than one electron bands, probably the result

of correlation effects. A model starting from single particle bands is able to explain many features of the spectra. The linear dependence of the photohole widths with energy below E_F may or may not be derived from single-particle theory.

B. Superconducting State

1. Measurement of the superconducting gap

The gap is a fundamental property of superconductivity. In the past, tunneling and infrared absorption were used to measure the gap in conventional superconductors. Photoemission was not applicable due to limited energy resolution. Since the gap is proportional to the transition temperature, in the high T_c superconductors, it became possible that the size of the gap may be comparable to the energy resolution that photoemission can achieve. Early photoemission attempts to measure the gap were generally inconclusive due to poor sample surfaces and inadequate resolution [62, 63]. About a year ago, several groups reported estimation of the gap in $Bi_2Sr_2CaCu_2O_8$ by photoemission. Imer et al. [64] performed experiments with high energy resolution (20 meV) but with angle integration, reporting a gap of $\Delta = 30$ meV. Manzke et al. [65] reported measurements with high angle resolution and moderate energy resolution. They also report a 30 meV gap.

We performed photoemission experiments with both high energy (32 meV) and angular (2°) resolution. The behavior of the states in a single band near Fermi level was studied both in the normal state

and superconducting state. Figure 20 shows EDCs taken at different emission angles, hence at different points in the Brillouin zone, at a temperature above T_c. As can be seen, at 11°, the band is well below Fermi level, and there is very little strength at the Fermi level. As we move out in the zone, the band disperses towards the Fermi level and at 18°, the band finally passes through the Fermi level. The inset of Fig. 20 shows a schematic of the dispersion of this band.

Figure 21 shows the EDCs taken in the same direction at 20K, a temperature well below T_c, with the normal state spectra superimposed. As can be seen, in the 11° spectra, there is very little change, except a slight sharpening of the edge, as the sample is cooled to 20K. As the band moves closer to the Fermi level, the change is dramatic. We note that the density of states at the Fermi level is pushed away from the Fermi level and piled up at higher binding energies. In fact, the remaining spectral weight at the Fermi level is the result of an asymmetric tail of the instrument function. The width of the pile-up peak is almost energy resolution limited. The angular resolution does not contribute much to the broadening because the band is flattened after a gap is opened.

To show the effect of the gap opening more clearly, we overlay the Fermi edge taken from the Pt foil on top of the spectra of $Bi_2Sr_2CaCu_2O_8$ at 90K and 20K, respectively (Fig. 22). It can be seen that the leading edge of the 90K spectrum lined up with the Pt edge nicely, while in the 20K spectrum, the leading edge apparently shifted to higher binding energies and there is a void in the density of states in the immediate vicinity of the Fermi level.

These spectra are repeatable as the sample is cycled between 20K
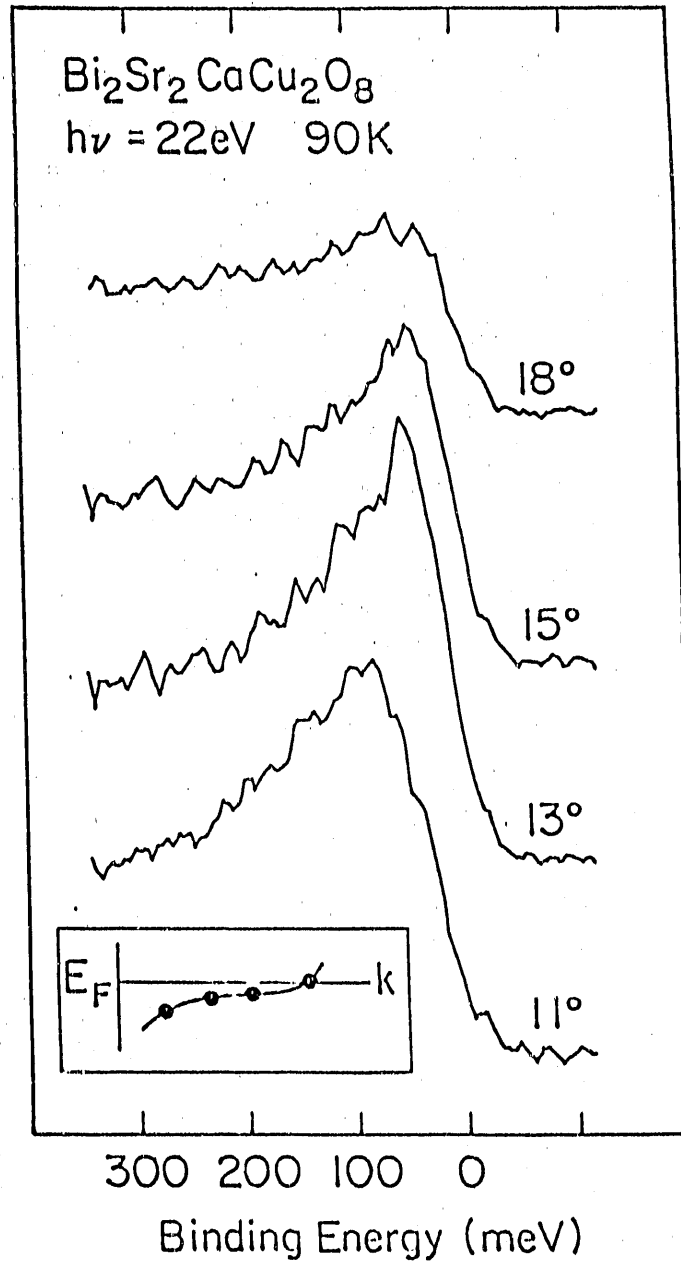
Fig. 20. Angle-resolved energy distribution curves for a surface of Bi₂Sr₂CaCu₂O₈ cleaved at 20K, but measured at 90K. The electron emission angles are marked. The inset shows schematically the motion of the initial state as the emission angle is changed

Fig. 21. Angle-resolved energy distribution curves for the sample of Fig. 20 cleaved and measured at 20K (heavier lines), with the 90K spectra of Fig. 20 superimposed with lighter lines

Fig. 22. Comparison of the Fermi edge of Pt with that of $Bi_2Sr_2CaCu_2O_8$ at 90K (top) and 20K (bottom)
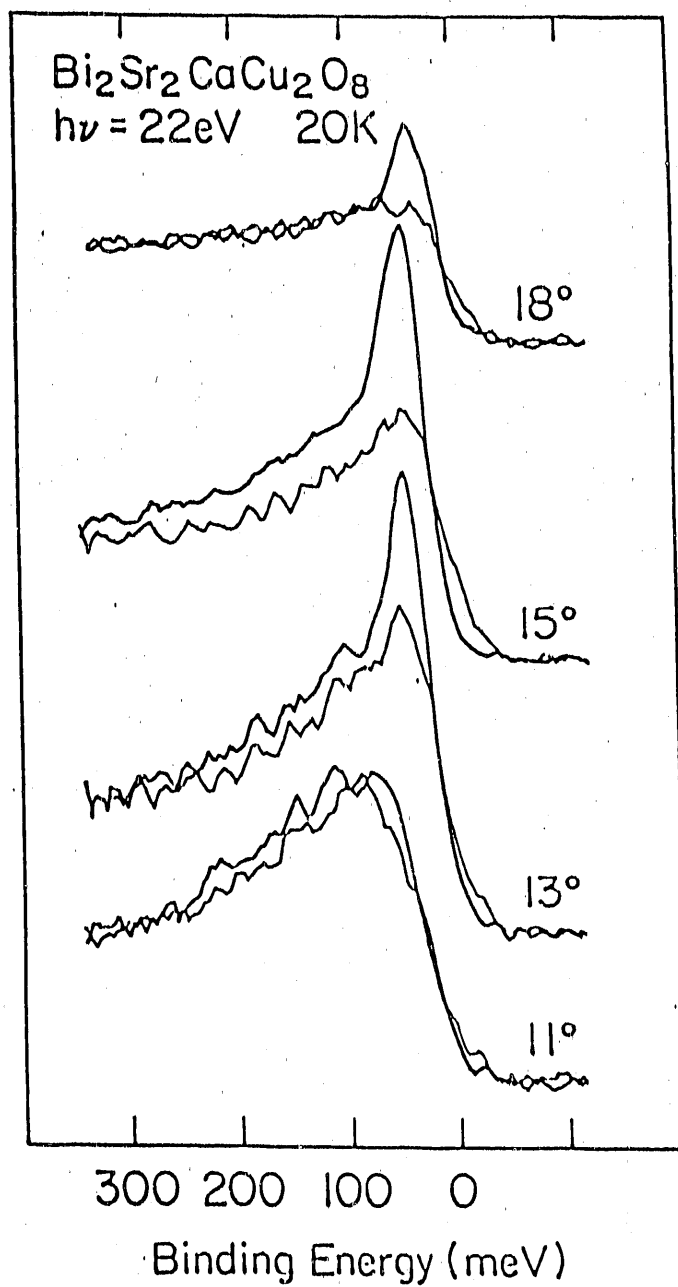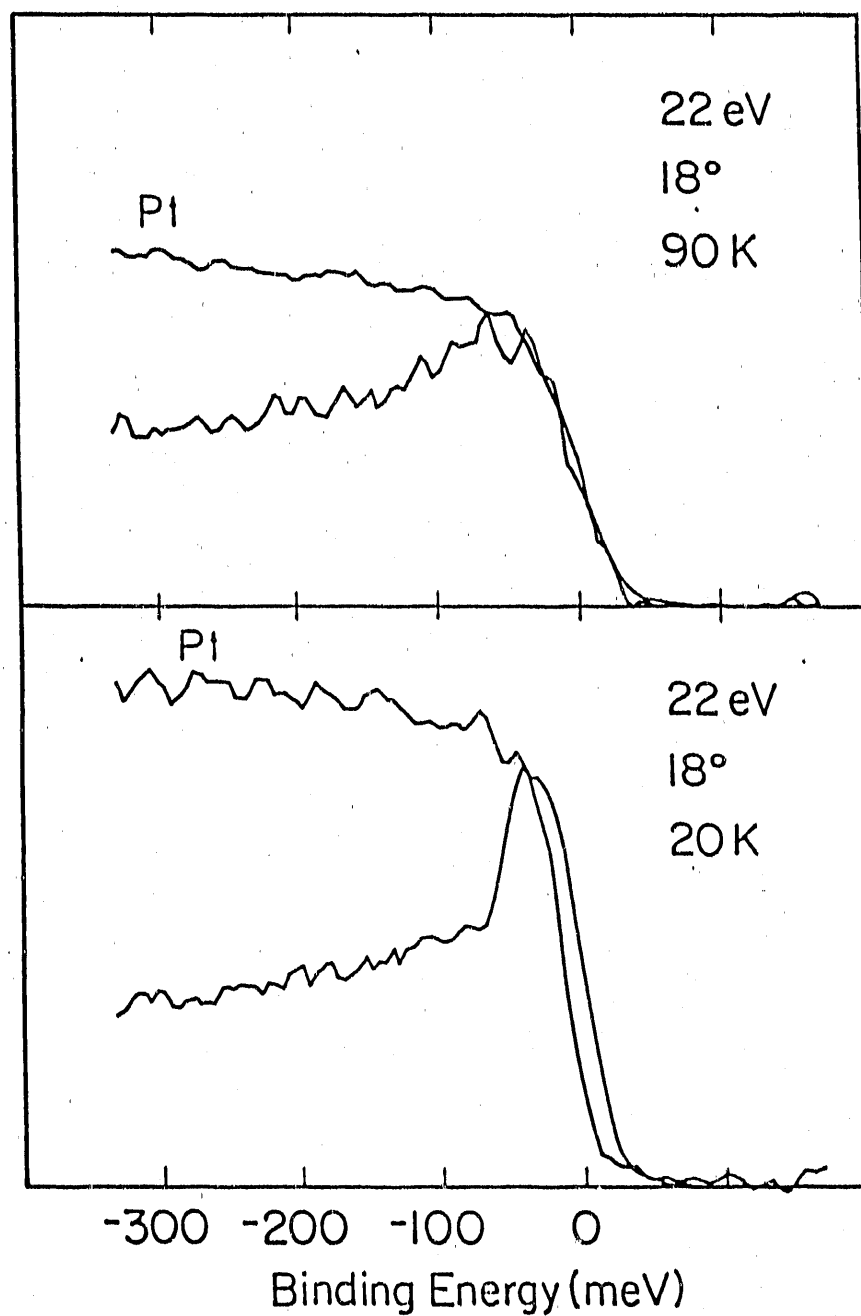
and 90K back and forth. Figure 23 shows EDCs taken at 15° at more temperature steps between 20K and 90K. It is clear that the spectral change is related to the superconducting transitions, not just a simple temperature effect. The temperature dependence of the gap will be discussed in more detail later.

The value of the gap cannot be obtained directly from the spectra. In order to extract a value for the gap, we have to model the states in the normal and superconducting state. To do this, we started with the 18° spectrum at 90K, where the band just crosses the Fermi level. A Lorentzian is assumed for the intrinsic peak and a linear term is used for the background. The sum of these two terms are then multiplied by the Fermi-Dirac function at 90K. Finally this is convolved with the instrument function. The instrument function is a skewed Gaussian with an asymmetric tail at the lower binding energy side. The Lorentzian width, strength, and the peak position are the important parameters in the fit. After a good fit is obtained, we go to the 20K spectrum. The peak position is not changed, but the width is reduced in order to have as much enhancement in the peak as observed in the experiment. Physically, the reduction in the width is the result of a decreased scattering rate and a less dispersive band due to the opening of a gap. (In the fitting, the strength is kept the same, thus the area is conserved.) The Fermi-Dirac function is now replaced by the BCS density of states, which has the form $\frac{|E|}{\sqrt{E^2 - \Delta^2}}$. Then, this is convolved with the same instrument function. The value of Δ is adjusted until a good fit resulted. The fitted curves are shown as the solid lines in Fig. 24. As can be seen, the fit is quite satisfactory. A gap $\Delta = 24$ meV was obtained. It is smaller than those reported by
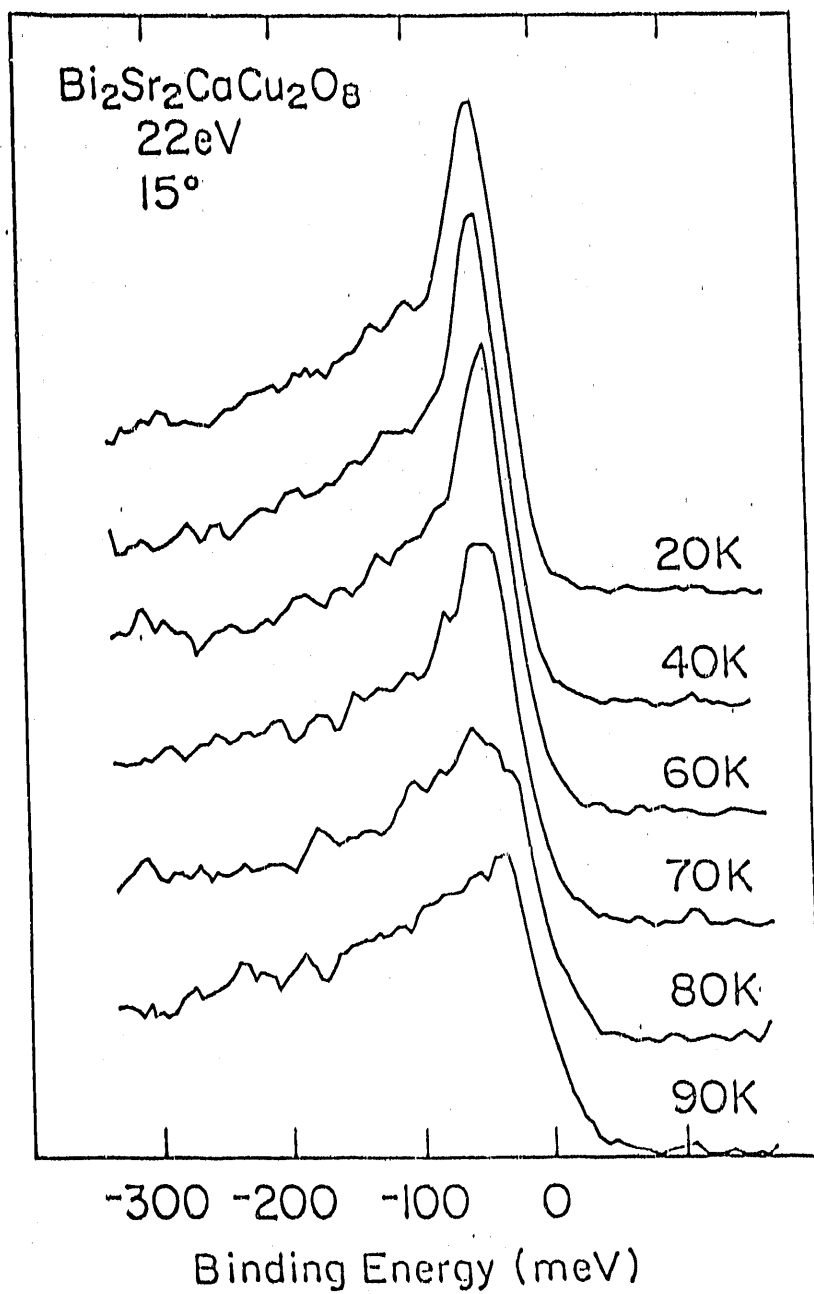
Fig. 23. Angle-resolved energy distribution curves for the surface of Fig. 20 taken at 15° at several temperatures below T_a and one above
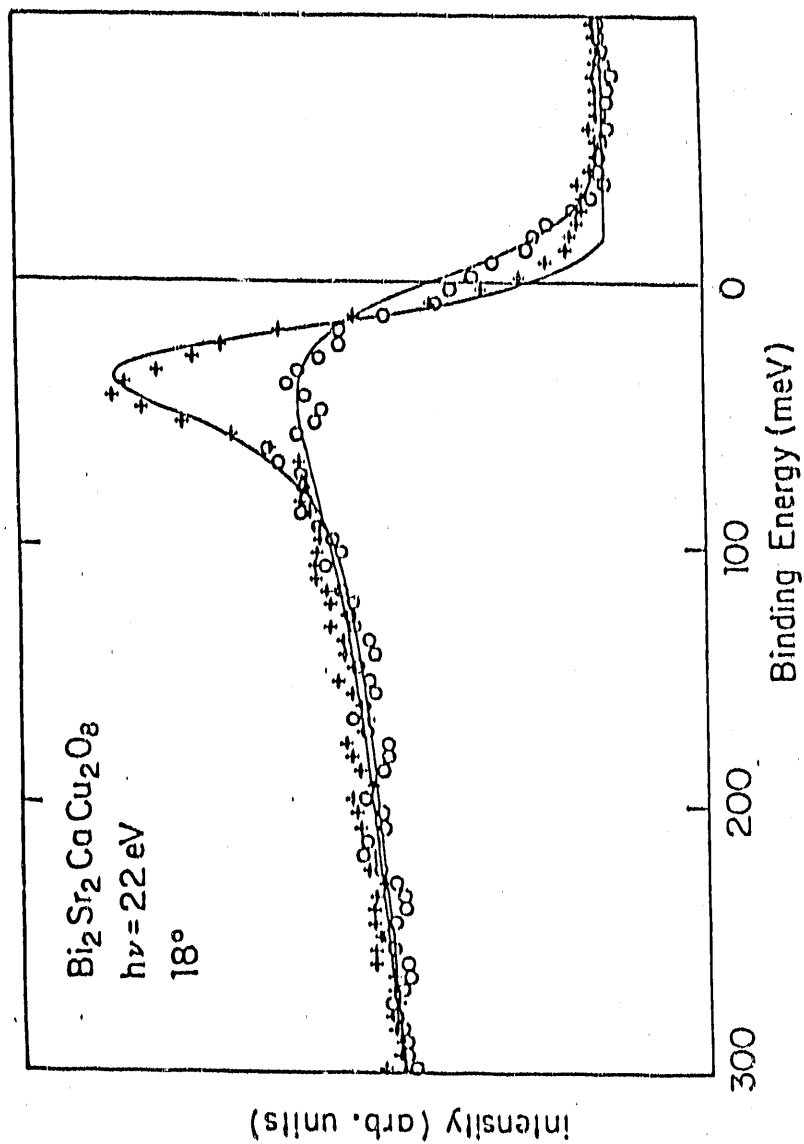
Fig. 24. Angle-resolved energy distribution curve for the surface of Fig. 20 taken at an angle of 18° at temperatures above and below T_c. The solid curves are the fits to the model described in the text. The binding energy of the Lorentzian is 33 meV and its width is 75 meV at 90K and 40 meV at 20K

other groups [64, 65], but the ratio $2\Delta/kT_c$ is still twice as big as the BCS theory predicts (7.0 vs. 3.52). The error in the fit is estimated to be ± 5 meV. Part of this error resulted from the uncertainty of the Fermi level due to the finite stability of the spectrometer.

At 18°, spectra were only measured at 20 and 90K, while at 15°, spectra were measured at many temperature steps, as shown in Fig. 23. It is clear that, at 15°, the band is below the Fermi level. As a result, when we model the spectra, the Lorentzian peak position is found to be at 55 meV below Fermi level, instead of 33 meV in the 18° spectra. Consequently, a gap of $\Delta = 34$ meV was obtained. We think that this reflects the inadequacy of the modeling when a band is below the Fermi level, and this number should not be taken seriously.

Although the absolute value of the gap obtained from the 15° spectra is not reliable, we think that the relation of gap vs. temperature measured at this angle should be qualitatively correct. The gaps extracted from each spectrum corresponding to different temperatures (Fig. 23) are shown as the solid dots in Fig. 25, and the weak-coupling BCS curve is shown as the solid line. As can be seen, the gap does not decrease as rapidly as the BCS theory predicts. This is consistent with the strong coupling case, since electrons are less likely to be thermally excited across the gap. Tunnelling measurements [66], however, obtained a temperature dependence of the gap which follows the BCS curve within error bars. It is surely desirable to make more careful photoemission measurements as a function of temperature at a point where the band just crosses the Fermi level.
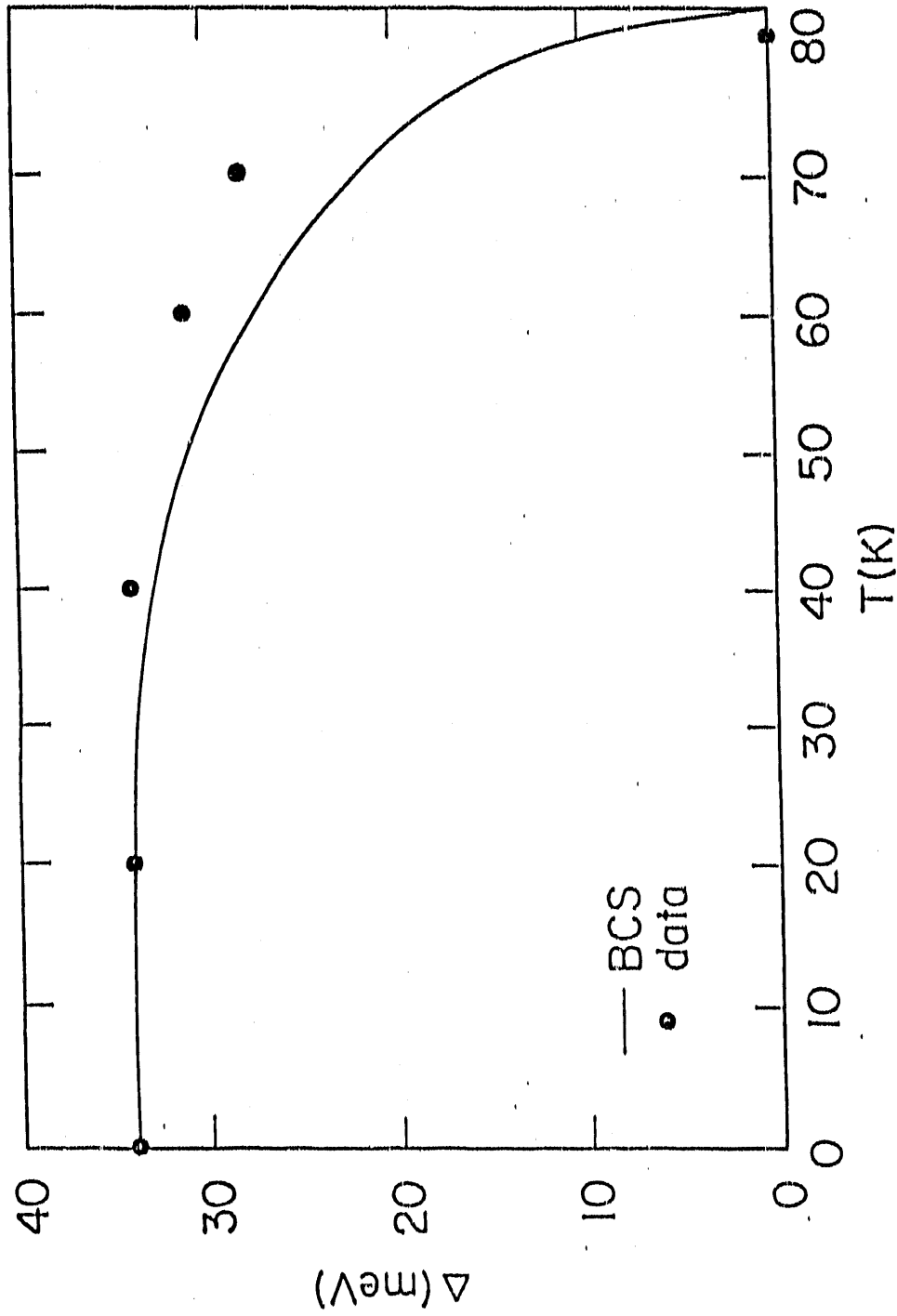
Fig. 25. Comparison of the superconducting gap as a function of temperature extracted from photoemission experiment (dots) and that of BCS theory (line)

2. Gap anisotropy?

The mechanism responsible for superconductivity in these cuprate high T_c superconductors is still not known. There are speculations that these materials may exhibit gap anisotropy. Tunneling [67] and infrared [68] measurements found evidence for gap anisotropy, in that the gap perpendicular to the basal plane is smaller than the gap in the basal plane. The anisotropy of the gap within the basal plane has been unknown. However, as far as the superconductivity mechanism is concerned, the later kind of gap anisotropy is more important. Many theories [69-72] exploring new superconductivity mechanisms, mostly in two dimensions, suggest d-wave pairing instead of conventional BCS s-wave pairing. As a result, the gap will have nodes in the Brillouin zone.

As described in the previous sections, angle-resolved photoemission is able to isolate the bands near the Fermi level in a small part of the zone and study the superconducting gap at each k-point on the Fermi surface. Due to the two-dimensional nature of the compound and the nature of the photoemission process, angle-resolved photoemission can only measure gaps in the plane, not perpendicular to the plane. Fortunately, the gap anisotropy in the plane is more relevant for the question of s-wave or d-wave pairing.

As described in the normal state studies, by measuring EDCs at a temperature above T_c as a function of angle, we can trace bands dispersing through the Fermi level, and determine the points at which they cross the Fermi level. To measure the gap, we measure EDCs at the crossing point at 90K (above T_c) and 20K (well below T_c) consec-

utively, and then extract the gap value by the modeling described in the previous section. Such careful measurements and modeling were made on several points on the Fermi surface, which are indicated as black dots in the Brillouin zone shown in Fig. 26. The same value for the gap is obtained at all these points. These points cover the Fermi surface on three major symmetry lines, namely the $\Gamma - X$, $\Gamma - Y$, and $\Gamma - \overline{M}$. According to band calculations, the former two regions have dominant Cu-O character, and the latter dominant Bi-O character [48]. In other parts of the zone where only 20K data were taken, the measured curves are consistent with this gap. We have not found with this or other samples, any point in the zone where the data would indicate zero or significantly smaller gap. Thus, we conclude that we find no evidence of gap anisotropy. This result should assist theorists in revealing the superconducting pairing mechanism in these materials.
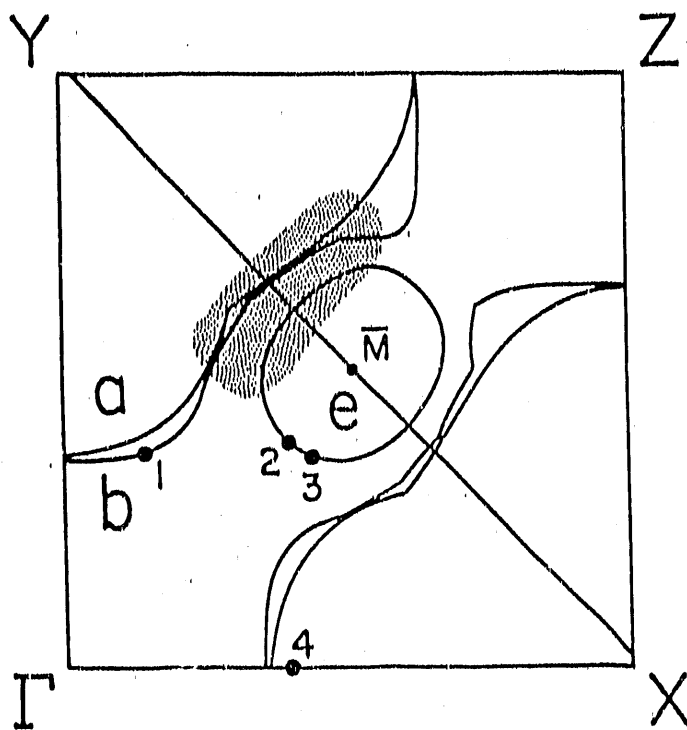
Fig. 26. Fermi surface of $Bi_2Sr_2CaCu_2O_8$ (from Ref. 48) showing points at which angle-resolved photoemission data were taken at both 20K and 90K

V. SUMMARY AND OUTLOOK

To summarize, our angle-resolved photoemission studies on $Bi_2Sr_2CaCu_2O_8$ revealed many details about the electronic structure of the high T_c material. For the normal state, we observed large band dispersion and a Fermi surface which is consistent with the one-electron band calculation. This evidence supports a Fermi liquid description of these materials. However, we also found subtle deviations from the Fermi liquid theory: the effective mass is heavier than the one-electron band calculation; the quasi-particle lifetime has a linear energy dependence rather than a quadratic dependence in normal Fermi liquids. For the superconducting state, a superconducting gap is seen, which is significantly larger than the gap for weak-coupling BCS materials. The gap is isotropic to within 5 meV in the a-b plane.

These results received considerable attention from many well-known theorists, and also generated some controversies on how to interpret the data. C. M. Varma et al. [56] proposed a phenomenological theory in which they claim that all the anomalous normal state behavior in high T_c materials can be derived under a single hypothesis. The linear energy dependence of the imaginary part of the self energy is part of the hypothesis. They characterize such a situation as "marginal Fermi liquid". Later, a corresponding microscopic theory based on an extended Hubbard model was given [73]. P. W. Anderson [58] took our data as strong support for his theory, in which the charge and spin are decoupled. His theory is a low dimensional Hubbard model. He characterized such a state as a "Luttinger liquid". G. A. Sawatzky [74] interpreted the intensity at higher binding energies

as an "incoherent continuum", which we regard as background. He argued that the fact that the incoherent continuum is not very well separated from the quasiparticle peak in the spectra and the peak asymmetry are the indications of strong interaction between electrons and other elementary excitations, such as phonons, magnons.

To further clarify these issues, more details of the spectral line shape and more careful data analysis are needed. Measurements with higher energy and angular resolution will certainly be very helpful. As better facilities become available, and samples with better homogeneity become available, more informative and reliable data can be expected.

Besides $Bi_2Sr_2CaCu_2O_8$, it should also be interesting to study some other classes of high T_c materials. Two particularly interesting groups of materials are the Y123 system, and the n-type superconductors. Technically, the 123 samples can be made more homogeneous. Their oxygen concentration can be controlled more accurately and their structure is relatively simple. According to band calculations, the bands near the Fermi level have more structures and are more complicated. It would be interesting to measure the superconducting gap in these materials. However, these studies can be more difficult because of their unstable surfaces at elevated temperatures.

VI. REFERENCES

1. J. G. Bednorz and K. A. Müller, Z. Phys. B 64, 189 (1986).

2. M. K. Wu, J. R. Ashburn, C. J. Torng, P. H. Hor, R. L. Meng, L. Gao, Z. J. Hwang, Y. Q. Wang, C. W. Chu, Phys. Rev. Lett. 58, 908 (1987).

3. H. Maeda, Y. Tanaka, M. Fukutomi, and T. Asano, Jpn. J. Appl. Phys. 27, L209 (1988); C. W. Chu, J. Bechtold, L. Gao, P. H. Hor, Z. J. Huang, R. L. Meng, Y. Y. Sun, Y. Q. Wang, and Y. Y. Xue, Phys. Rev. Lett. 60, 941 (1988).

4. Z. Z. Sheng, A. M. Hermann, A. El Ali, C. Almasan, J. Estrada, T. Datta, and R. J. Matson, Phys. Rev. Lett. 60, 937 (1988).

5. Y. Tokura, H. Takagi and S. Uchida, Nature 337, 345 (1989).

6. S. Martin, A. T. Fiory, R. M. Fleming, L. F. Schneemeyer, and J. V. Waszczak, Phys. Rev. Lett. 60, 2194 (1988).

7. G. Briceno, and A. Zettl, Solid State Commun. 70, 1055 (1989).

8. R. T. Collins, Z. Schlesinger, F. Holtzberg, and C. Field, Phys. Rev. Lett. 63, 422 (1989).

9. J. Friedel, J. Phys.: Condens. Matter. 1, 7757 (1989).

10. J. Bardeen, L. N. Cooper, and J. R. Schrieffer, Phys. Rev. 108, 1175 (1957).

11. L. N. Cooper, Phys. Rev. 104, 1189 (1956).

12. G. M. Eliashberg, Zh. Eksp. Teor. Fiz. 38, 966 (1966)(Sov. Phys.-JETP 11, 696 (1960)); P. B. Allen and B. Mitrovic, in "Solid State Physics", H. Ehrenreich, F. Seitz, and D. Turnbull, eds. (Academic Press, New York, 1982), p. 2-92.

13. W. E. Pickett, H. Krakauer, D. A. Papaconstantopoulos, and L.

L. Boyer, Phys. Rev. B 35, 7252 (1987).

14. N. F. Mott, Proc. Phys. Soc. Sect. A 62, 416 (1949); G. A. Sawatzky, and J. W. Allen, Phys. Rev. Lett. 53, 2339 (1985); J. Zaanen, G. A. Sawatzky, and J. W. Allen, Phys. Rev. Lett. 55, 418 (1985); A. Fujimori, and F. Minami, Phys. Rev. B 30, 957 (1984).

15. J. A. Yarmoff et al. Phys. Rev. B 36, 3967 (1987); P. D. Johnson, et al. Phys. Rev. B 35, 8811 (1987).

16. P. W. Anderson, Science, 235, 1196 (1987).

17. R. B. Laughlin, Science, 242, 525 (1988).

18. A. J. Arko, R. S. List, C. G. Olson et al. J. Magn. Magn. Mater. 75, L1 (1988).

19. L. C. Smedskjaer, J. Z. Liu, R. Benedek, D. G. Legnini, D. J. Lam, M. D. Stahulak, H. Claus and A. Bansil, Physica C 156, 269 (1988).

20. H. Alloul, T. Ohno, and P. Mendels, Phys. Rev. Lett. 63, 1700 (1989).

21. A. Einstein, Annalen Physik 17, 132 (1905).

22. C. N. Berglund and W. E. Spicer, Phys. Rev. 136, A1030 (1964).

23. C. J. Powell, Surf. Sci. 44, 29 (1974).

24. I. Lindau and W. E. Spicer, J. Electron Spectrosc. and Relat. Phenom. 3, 409 (1974).

25. M. P. Seah, W. A. Dench, Surf. and Interface Anal. 1, 2 (1979).

26. R. C. G. Leckey, Appl. Surf. Sci. 13, 125 (1981).

27. I. Adawi, Phys. Rev. A 134, 788 (1964).

28. G. D. Mahan, Phys. Rev. B 2, 4334 (1970); Phys. Rev. Lett. 24, 1068 (1970).

29. W. L. Schaich and N. W. Ashcroft, Phys. Rev. B 3, 2452 (1971).

30. P. J. Feibelman and D. E. Eastman, Phys. Rev. B 10, 4932 (1974).

31. J. B. Pendry, Surf. Sci. 57, 679 (1976); J. B. Pendry and J. F. L. Hopkinson, Computer Phys. Commun. 19, 69 (1980).

32. B. W. Holland, Surf. Sci. 68, 490 (1977).

33. H. Z. Bross, Z. Phys. B 28, 173 (1977).

34. T. C. Chiang, J. A. Knapp, M. Aono and D. E. Eastman, Phys. Rev. B 21, 3515 (1980).

35. J. B. Pendry, in "Photoemission and the Electronic Properties of Surfaces", ed. by B. Feuerbacher, B. Fitton, and R. F. Willis (J. Wiley and Sons, New York, 1978), p. 94.

36. N. W. Ashcroft and N. D. Mermin, in "Solid State Physics", (Holt, Rinehart and Winston, New York, 1976), p. 346.

37. D. Pines, in "Many-body Problem" (W. A. Benjamin, Inc., New York, 1962).

38. O. Gunnarsson, K. Schönhammer, Phys. Rev. B 28, 4315 (1983); Phys. Rev. B 31, 4815 (1985).

39. G. A. Sawatzky and J. W. Allen, Phys. Rev. Lett. 53, 2339 (1985).

40. Z.-X. Shen et al. Phys. Rev. B 36, 8814 (1987).

41. M. Rowe, Nucl. Instrum. Methods B 24/25, 414 (1987).

42. C. G. Olson, Nucl. Instum. Methods A 266, 205 (1988).

43. VSW HA50 Hemispherical Analyzer Instruction Manual, England, 1989.

44. J. M. Tarascon et al., Phys. Rev. B 37, 9382 (1988).

45. S. Sunshine et al., Phys. Rev. B 38, 893 (1988).

68

46. R. M. Hazen et al., Phys. Rev. Lett. 60, 1657 (1988).

47. W. E. Pickett, Rev. Mod. Phys., 61,433 (1989).

48. S. Massidda, J. Yu, and A. J. Freeman, Physica C 52, 251 (1988).

49. H. Krakauer and W. E. Pickett, Phys. Rev. Lett. 60, 1665 (1988).

50. L. F. Mattheiss and D. R. Hamann, Phys. Rev. B 38, 5012 (1988).

51. M. S. Hybertsen and L. F. Mattheiss, Phys. Rev. Lett. 60, 1661 (1988?).

52. P. C. Pattnaik and D. M. Newns, Phys. Rev. B 41, 880 (1990).

53. R. Manzke, T. Buslaps, R. Claessen, M. Skibowski, and J. Fink, Physica C 162-164, 1381 (1989).

54. J. M. Luttinger, Phys. Rev. 119, 1153 (1960).

34. T. C. Chiang, J. A. Knapp, M. Aono, and D. E. Eastman, Phys. Rev. B 21, 3515 (1980).

55. B. J. Slagsvold, J. K. Grepstad, and P. O. Gartland, Physica Scripta T4, 65 (1983).

56. C. M. Varma, P. B. Littlewood, S. Schmitt-Rink, E. Abrahams, and A. E. Ruckenstein, Phys. Rev. Lett. 63, 1996 (1989).

57. A. Virosztek and J. Ruvalds, preprint, submitted to Phys. Rev. Lett.

58. P. W. Anderson, manuscripts submitted and private communication.

59. C. G. Olson, R. Liu, D. W. Lynch, B. W. Veal, Y. C. Chang, P. Z. Jiang, J. Z. Liu, A. P. Paulikas, A. J. Arko, R. S. List, Physica C 162-164, 1697 (1989).

60. D. L. Huber, Solid State Commun. 68, 459 (1988).

61. Y. Chang, M. Tang, Y. Hwu, M. Onellion, D. L. Huber, G. Margaritondo, P. A. Morris, W. A. Bonner, J. M. Tarascon, and N. G. Stoeffel, Phys. Rev. B 39, 7313 (1989).

62. E. R. Moog, S. D. Bader, A. J. Arko et al., Phys. Rev. B 36, 5583 (1987).

63. Y. Chang, M. Tang et al., Phys. Rev. B 39, 4740 (1989).

64. J. -M. Imer, F. Patthey, B. Dardel, W.-D. Schneider, Y. Baer, Y. Petroff, and A. Zettl, Phys. Rev. Lett. 62, 336 (1989).

65. R. Manzke, T. Buslaps, R. Claessen, and J. Fink, Europhysics Lett. 9, 477 (1989).

66. M. Lee, D. B. Mitzi, A. Kapitulnik, and M. R. Beasley, Phys. Rev. B 39, 801 (1989).

67. G. Briceno and A. Zettl, Solid State Commun. 70, 1055 (1989).

68. R. T. Collins, Z. Schlesinger, F. Holtzberg, and C. Field, Phys. Rev. Lett. 63, 422 (1989).

69. M. Cyrot, Solid State Commun. 62, 821 (1987).

70. A. E. Ruckenstein, P. J. Hirschfeld, and J. Appl. Phys. Rev. B 36, 857 (1987).

71. G. Kotliar, Phys. Rev. B 37, 3664 (1988).

72. J. R. Schrieffer, X. G. Wen, and S. C. Zhang, Phys. Rev. B 39, 11663 (1989).

73. C. M. Varma, Bull. Am. Phys. Soc. 35, 274 (1990).

74. G. A. Sawatzky, Nature, 342, 480 (1989).

70

VII. ACKNOWLEDGMENTS

First, I would like to thank my advisor, Dr. David Lynch. During the years of my graduate study, he introduced me to many interesting subjects, and constantly guided me in the process of pursuing these subjects. The research experience I gained and any accomplishment I made in these years are due to his insights, guidance and encouragement.

I want to express special thanks to Dr. Clifford Olson, who is the principal investigator of the work described in this thesis. I am grateful for the opportunity to work with such a highly experienced scientist, and the opportunity of being involved in this exciting work. The one year I spent with Dr. Olson at the Synchrotron Radiation Center was extremely rewarding.

I would like to thank my husband, Yi Wan, for his love, support and encouragement. The constant discussion about my work and physics in general was so helpful and inspiring. I cannot imagine how I could go through the graduate study without him.

I would like to thank Dr. Zaffarano and Mrs. Zaffarano, Dr. Binlin Young and Mrs. Young, for their hospitality and help when I first arrived in Ames, and care for me over the years. I also want to thank other faculty, staff and friends in physics department, who made my years in Ames very enjoyable.

Finally, I want to thank my parents, Zhaorui Liu and Zhaohua Wu, for their love and their efforts in my upbringing.

This work was performed at Ames laboratory under contract No. W-7405-eng-82 with the U. S. Department of Energy. The United

States government has assigned the DOE Report number IS-T 1410 to this thesis.

- END -

DATE FILMED

10 / 23 / 90